Near-Surface Characterization of the Lisbon and Lower Tagus Valley Area, Portugal, for Seismic Hazard Assessment: V-S30 and Soil Classification Maps

Carvalho, J.; Dias, R.; Ghose, R.; Teves-Costa, P.; Borges, J.; Narciso, J.; Pinto, C.; Leote, J.

DOI
10.1785/0120170340

Publication date
2018

Document Version
Final published version

Published in
Bulletin of the Seismological Society of America

Citation (APA)
Carvalho, J., Dias, R., Ghose, R., Teves-Costa, P., Borges, J., Narciso, J., Pinto, C., & Leote, J. (2018). Near-Surface Characterization of the Lisbon and Lower Tagus Valley Area, Portugal, for Seismic Hazard Assessment: V-S30 and Soil Classification Maps. *Bulletin of the Seismological Society of America*, *108*(5A), 2854-2876. https://doi.org/10.1785/0120170340

Bulletin of the Seismological Society of America, Vol. 108, No. 5A, pp. 2854–2876, October 2018, doi: 10.1785/0120170340

Near-Surface Characterization of the Lisbon and Lower Tagus Valley Area, Portugal, for Seismic Hazard Assessment: V_{S30} and Soil Classification Maps

by J. Carvalho, R. Dias, R. Ghose, P. Teves-Costa, J. Borges, J. Narciso, C. Pinto, and J. Leote

Abstract The Lower Tagus Valley (LTV) region includes the metropolitan area of Lisbon and has the highest population density in Portugal, with about 3.5 million inhabitants. The LTV has been struck by several historical earthquakes that caused significant economic and human losses, and therefore, earthquake damage mitigation is of great importance. The present research was directed toward preparation of the first detailed V_{S30} and soil classification maps for the LTV region using *in situ* shear-wave velocity (V_S) measurements. These maps were built using *P*- and *S*-wave seismic velocities in the shallowest surface, obtained mostly from seismic refraction and a few crosshole datasets, together with lithostratigraphic studies and analyses of boreholes drilled for water supply and geotechnical investigations. Borehole data were used to confirm layer thicknesses and lithologies, and to overcome the limitations of traditional refraction interpretation. Our results (V_{S30} and soil classification maps) show that lithological changes within each formation prevent simple generalization of geophysical data/interpretations based solely on geological mapping. Contrary to previously available V_{S30} maps based on proxies or gross geological generalizations, different classes are obtained inside the Holocene alluvial sediments and the Miocene units, for instance. Certain areas with Miocene outcropping, such as the district capital of Santarém, unexpectedly fall into a moderate risk class, albeit showing hard-rock outcrops. Though there is scope for further improvements in the future, the maps presented results from the first rigorous near-surface characterization campaign undertaken in the region. Velocity information assembled in this work can be further used to correct earthquake records from a number of seismological stations and to update velocity models used in ground-motion simulations. Furthermore, seismic refraction interpretation was compared among different acquisition geometries for seismic noise measurements at three geologically distinct sites to evaluate the use of these techniques for future *S*-wave data acquisition.

Introduction

The Lower Tagus Valley (LTV) region (Fig. 1, dashed rectangle) has been struck by multiple destructive earthquakes. The quest for the source location of these earthquakes is still a matter of debate (e.g., Grandin *et al.*, 2007a,b; Carvalho *et al.*, 2011; Besana-Ostman *et al.*, 2012; Gutscher *et al.*, 2012; Cabral *et al.*, 2013; Baptista *et al.*, 2014). Two main source areas are the Eurasia–Africa plate boundary, which is capable of producing large earthquakes such as the 1755 (M_s 8.5–9; e.g., Baptista and Miranda, 2009) or the 1969 (M_s 8.0; e.g., Buforn *et al.*, 1988) events, and the local LTV active fault system, which very probably produced the 1344, 1531, and 1909 earthquakes (e.g., Besana-Ostman *et al.*, 2012; Cabral *et al.*, 2013; Borges *et al.*, 2015; Canora *et al.*, 2015), among others. Though the return period for earthquakes for the individual faults is large (see e.g., Carvalho *et al.*, 2006; Vilanova *et al.*, 2014), clusters of earthquakes at a much shorter time range (a few hundreds of years) do occur (Carvalho *et al.*, 2006).

The LTV region includes the metropolitan area of Lisbon and represents around 2.8 million people in the city of Lisbon (the capital of Portugal) itself, and also includes the Península of Setúbal, where the district capital Setúbal is located, and a part of the districts of Leiria and Santarém (see Fig. 2), totaling about 3.5 million inhabitants. Given its central location, the region comprises important Portuguese communication routes and houses multiple critical facilities. The seismic hazard assessment and earthquake damage mitigation of the region are, therefore, very important.

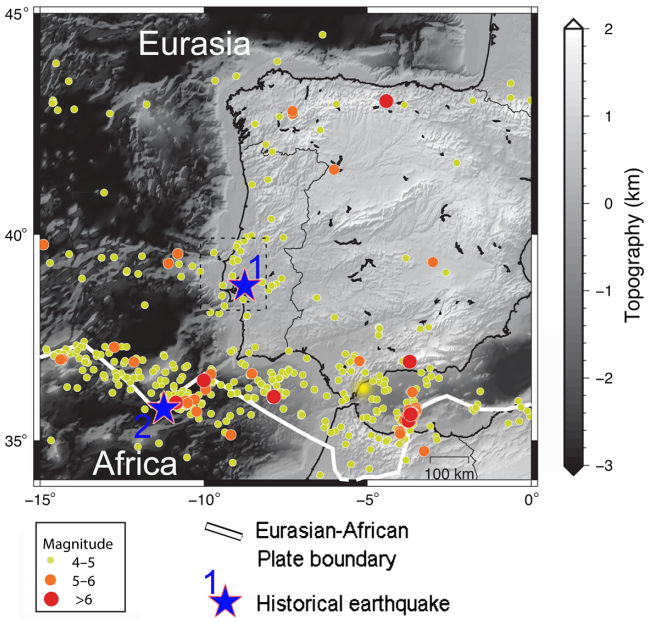

Figure 1. Location (indicated by black dashed rectangle) and seismotectonic setting of the Lower Tagus Valley study area. Seismicity for the period 1962–2018 after the Portuguese Institute for the Sea and Atmosphere, showing earthquakes with magnitudes > 4. Stars denote probable epicenter location of historical damaging earthquakes: 1: 1344, 1531, and 1909 earthquakes; 2: 1755 and 1969 events (see Introduction). Plate boundary geometry after Bird (2003). The color version of this figure is available only in the electronic edition.

The importance of site effects in the evaluation of earthquake shaking and damage potential is well recognized. For investigations of site effects, the dynamic characterization of the most surficial layers of the subsoil is required. Near-surface *P*- and *S*-wave seismic velocities provide important information for studying ground motion, natural frequency of vibration, and liquefaction potential (e.g., Fumal and Tinsley, 1985; Bauer *et al.*, 2001).

Several authors have previously recognized the importance of the thick Cenozoic cover that blankets a part of the LTV region (e.g., Carvalho *et al.*, 2006), the seismic-wave amplitude amplifications caused by this Cenozoic cover (Borges *et al.*, 2015), and the local site effects controlling the seismic intensities observed during the historical earthquakes (e.g., Teves-Costa and Batló, 2011).

V_{S30} is a useful and traditionally used parameter in site-effect studies. It is defined as the time weighted average of the inverse of the seismic shear-wave velocity from the surface down to a depth of 30 m (e.g., Borcherdt, 2012). Carvalho *et al.* (2013) presented tentative V_{S30} and soil classification maps for the study region. They used only 34 *P*- and *S*-wave measurements and recognized the difficulty of generalizing/extending the data points to the geological polygons at a 1:500 K or 1:1 M scale due to lithological and facies variations inside each geological formation, and therefore, they showed only maps with colored data points. Teves-Costa *et al.* (2013) also presented a V_{S30} map for the LTV region at a 1:1000 K scale, but used only 10 data points and a gross geologically based generalization of the data points, whereas Silva *et al.* (2015) published V_{S30} maps of Portugal using proxies and no real *S*-wave measurements. In this work, we carry out near-surface characterization of the LTV region based on geophysical (primarily *P*- and *S*-wave velocities), geological, and borehole data for seismic hazard analysis and mitigation of damage due to earthquakes.

In the present research, a detailed V_{S30} map and a soil classification map based on Eurocode 8 for civil engineering (Eurocode 8, 2004) are, for the first time, produced for the study region using 1:1 M scale geological maps. The data points (V_{S30} measurements and estimated soil type) are generalized to the digital 1:1 M scale cartography using a geological approach. In this generalization, information from 1:50 K scale geological maps and unpublished lithostratigraphic and geophysical datasets were used. The generalization process is explained in more detail in the Deriving V_{S30} and Soil Classification Maps section.

The seismic refraction method was used in the present research to estimate *P*- and *S*-wave seismic velocities, while borehole information and *in situ* geological and lithological studies were performed to corroborate layer depths and lithologies. A total of 41 *S*-wave and 41 *P*-wave refraction profiles were acquired between 2011 and 2013. Another 36 previously acquired *P*-wave refraction profiles (in J. Carvalho, unpublished data, 1997, see Data and Resources) were used to get *S*-wave velocities using V_P/V_S ratio (*P*- and *S*-wave velocity ratio) obtained from more recent datasets. The old *P*-wave profiles were acquired using a similar geometry and were also located close to boreholes to check if the investigation depth had been reached and to corroborate the interpretation. Two *P*- and *S*-wave crosshole measurement datasets from an engineering construction site and three other downhole measurements (Teves-Costa *et al.*, 2014) were further appended. At three different sites, the refraction results were compared with different seismic noise measurements to assess the feasibility of this methodology to acquire more *S*-wave data in the future (see Appendix B).

V_{S30} distribution and a soil classification based on the Eurocode 8 (2004) were obtained from *S*-wave velocity, layer thickness, and standard penetration test (SPT) information. The equivalence of Eurocode 8 with other codes (Building Seismic Safety Council [BSSC], 1994; International Council of Building Officials [ICBO], 1997) is supplied. This soil classification and V_{S30} maps will be based on 82 velocity data points and generalized to a geological map at the scale of 1:1 M (Laboratório Nacional de Energia e Geologia [LNEG], 2010) using unpublished lithostratigraphic information. Both maps will be useful in engineering, designing critical facilities, and land planning, and will also provide important information for site-effect studies and mitigation of earthquake-induced damage in the region. The results presented will also serve multiple goals in the future: (1) estimating the distribution of V_P/V_S ratio and hence Poisson's ratio, and other geomechanical parameters that

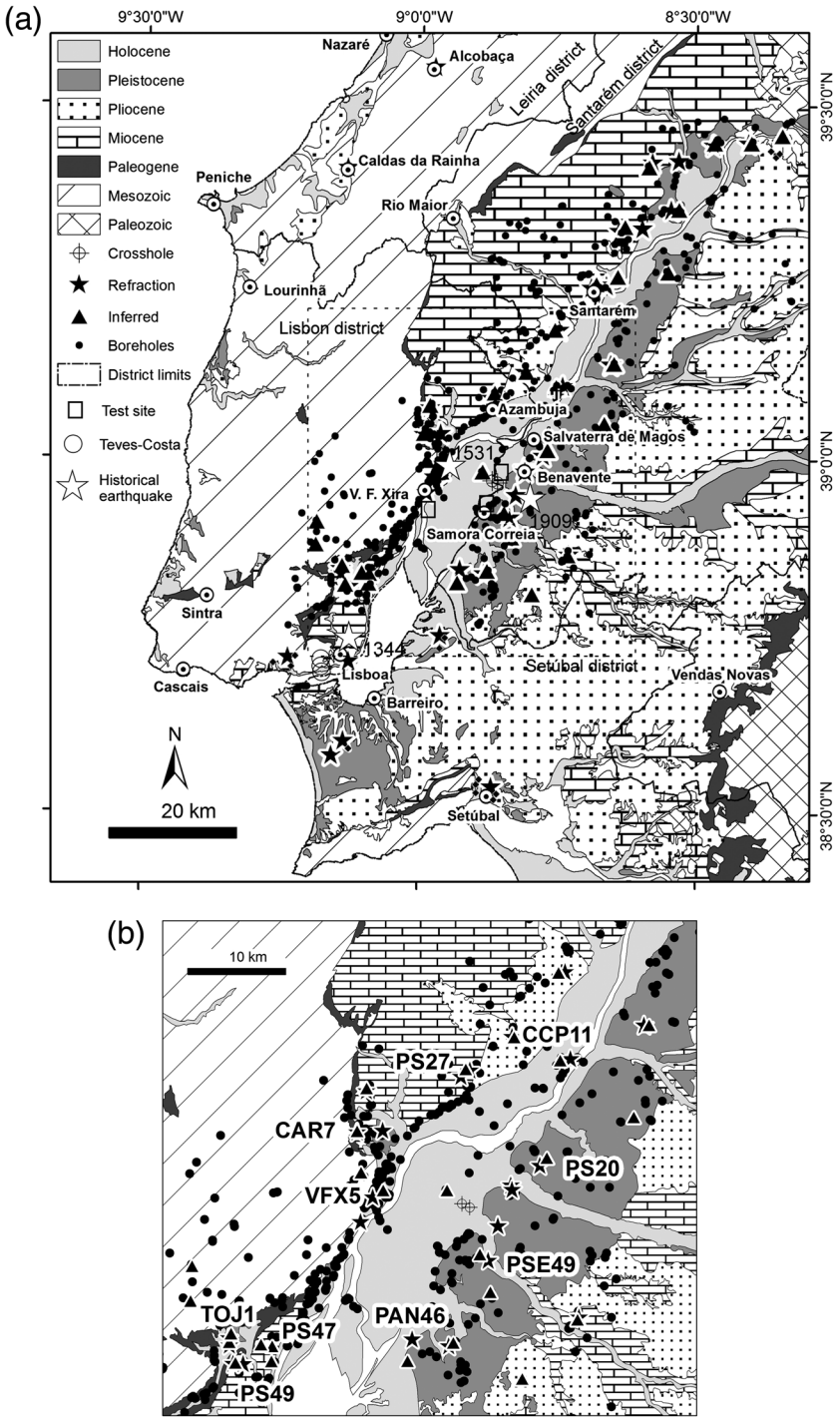

Figure 2. (a) Location of the 41 *S*-wave refraction profiles acquired in the present research (filled stars), 34 old *P*-wave profiles from which V_S was calculated (filled triangles), and 2 crosshole measurements at an engineering construction site (circled cross). The profiles have been plotted over a simplified geological map at the 1:1 M scale where geological formations mapped at the 1:50 K scale were grouped by Epoch (adapted from Laboratório Nacional de Energia e Geologia [LNEG], 2010). The dashed rectangle indicates the area zoomed in (b). Large, numbered stars indicate epicenter location and the date of local historical earthquakes. Test sites where seismic noise (see Appendix B) and crosshole measurements were available to compare with the seismic refraction data are marked by open squares. Three data points published by Teves-Costa *et al.* (2014) are indicated by open circles. Boreholes are indicated by filled circles. LTCB, Lower Tagus Cenozoic basin; LB, Lusitanian basin (Mesozoic). (b) Close-up of the central region of (a).

are useful in site-effect studies; (2) correcting earthquake records at seismological stations of the Portuguese national seismic network (as the velocity data points acquired here are located very close to the location of a number of seismological stations, see Veludo *et al.*, 2017, for location of the Portuguese seismic network); (3) upgrading the existing velocity models used in simulations of strong motion (Grandin *et al.*, 2007a,b; Borges *et al.*, 2015); and (4) allowing the use of higher frequencies in modeling.

Geological Setting

The LTV region is affected by the tectonic activity in the generally east–west-trending Eurasia–Africa plate boundary. Figure 2 shows a simplified geological map of the study region at the 1: 1 M scale, where the geological formations of a particular age (that are mapped at the 50 K scale) have been grouped. A part of the study region is a vast area called the Lower Tagus Cenozoic basin (LTCB)—characterized by Paleogene and younger deposits, which are surrounded by the Mesozoic sediments of the Lusitanian basin (LB) to the west and by the pre-Mesozoic igneous and metamorphic rocks outcrop to the east (Paleozoic in Fig. 2).

From a stratigraphic point of view, the LTV region is underlain by a basement constituted of Paleozoic and Proterozoic igneous and metamorphic rocks, overlain by a Meso-Cenozoic cover. Jurassic sediments are vastly dominated by carbonates of the Montejunto, Brenha (and Candeeiros Formation, lateral equivalent of Brenha Formation), and Coimbra Formations, siliciclastic Abadia Formation, sandstones and carbonates of the Freixial, Sobral, and Arranhó Formations, whereas Cretaceous formations comprise the Alcabideche, Alcântara, and Torres Vedras/Cascais carbonates and sandstones (see e.g., stratigraphy in Carvalho *et al.*, 2005). The sediment cover is disrupted by Jurassic basic dikes, a Late Cretaceous intrusion (Sintra massif), and the volcano-sedimentary complex of Lisbon (LNEG, 2010). The lowermost deposits of the LTCB that outcrop at the borders of the basin consist of 200–400-m-thick continental Paleogene sedimentary rocks. The maximum thick-

ness of the Paleogene units estimated from the interpretation of seismic and well data is about 500 m, with an average thickness of 200–300 m; these sedimentary rocks do not show important thickness variations. Paleogene sediments comprise continental conglomerates, sandstones, silt-stones, and claystones (Pais *et al.*, 2012).

The stratigraphy/geology of the Neogene mapped at the 1:50 K scale is described in the following paragraphs. During the Miocene, over 800 m of continental and shallow-marine sediments accumulated in depocenters (Cabral *et al.*, 2003). Miocene geological units include, in the central sector of LTCB, sandstones and clays (Alcoentre Formation) of Early and Middle Miocene, and swamp and lacustrine carbonates (Almoster Formation) that pass laterally into clay bodies with the development of carbonate crusts; that is, beds of carbonate rocks formed by precipitation that can also occur as concretions within sediments (Tomar Clays Formation) from the Upper Miocene (Pais *et al.*, 2012). The distal southwest sector of LTCB includes shallow-marine sediments, marls with marine microfossils, and highstand prograding deposits generally designated as the Lisbon Miocene (Pais *et al.*, 2012); this comprises the Musgueira limestones, Banco Real, Marvila Limestones, Areolas de Braço de Prata, Sands with Placuna miocénica, and Vale de Chelas Sands formations. . The Pliocene units, mainly constituted of sands and clayey or silty sands (Ulme Formation) and conglomerates, and sands (Almeirim Formation) of Late Pliocene to Pleistocene, do not exceed 300 m of thickness (Pais *et al.*, 2012). Pleistocene outcrops include the fluvial terraces deposits formation composed of sands and clays topped with beds of pebbles, and the undifferentiated sands and gravels formations. During the Holocene, alluvial sediments (muds and sands) were deposited by the Tagus River.

Seismic Velocity/Depth Data

New Seismic Refraction Profiles: Data Acquisition and Interpretation

The location of the seismic refraction profiles was selected to sample all the geological formations present in the study region and their distinct lithologies. For the exact location of the profiles, surface geology, logistics, the location of existing geotechnical soundings, water supply wells, and previously acquired *P*-wave profiles (see the Use of Old *P*-Wave Refraction, SPT, and Crosshole Datasets section) were taken into consideration. Surface geology and lithology were chosen using 1:50 K geological maps and were confirmed at each location by a detailed geological survey. All Neogene and Quaternary geological formations were sampled at least once. A total of 41 locations were selected, which are shown in Figure 2.

V_{S30} estimation requires an investigation depth of about 30 m. Next, a discussion on the investigation depth reached by the approach used most often in this work to obtain V_{S30} data, the refraction method, is presented. The receiver spread length with the refraction method usually varies between 2 and 10 times the required investigation depth (e.g., Rafek, 1989; ASTM International, 2000; Hunt, 2006; Knödel *et al.*, 2007; Maunde and Bassey, 2017), depending on the velocity structure and assuming that the seismic source was strong enough to produce enough energy to allow picking of the first breaks at the furthest receivers. In this research, a total profile length of 84 m was used, with 24 vertical and 24 horizontal receivers spaced 3.5 m apart. Later on, we show that this geometry was adequate to reach the required 30 m investigation depth. Two off-end shot gathers and three shot gathers inside the receiver array located 21 m apart were acquired to achieve a reasonable control on the velocity of the uppermost low-velocity layer. The nearest source receiver offset was of 1.75 m. The seismic traces were sampled at every 0.12 ms. This was necessary for a reliable picking of the first arrivals in the shallow refraction datasets (Palmer, 1981). As seismic source, a metal hammer and a plate were used in *P*-wave surveys and a 3-m-wide wooden beam hit horizontally at both sides with a metal hammer as the *S*-wave source. The wooden joist was coupled to the ground by the wheels of a jeep.

A common practice in *S*-wave data acquisition is to sum the data from strikes from the opposite sides of the seismic source to reduce *P*-wave contamination. In the present research, we opted to use strikes from both sides of the wooden beam, then plotted them side by side and compared them to ascertain the first arrivals. This eliminated the possible incoherent noise, increased the confidence in our picking, and allowed for error estimations. Figure 3 shows some examples of the acquired raw shot gathers. The Society of Exploration Geophysicists (SEG) polarity convention was used, in which an impact produced a downswing (Fig. 3a) in the first arrivals in *P*- and *S*-wave datasets. The base of the horizontal geophones for transverse strikes was oriented in the crossline direction.

The first-arrival picking was carried out using raw and band-pass filtered shot records, which were displayed at different horizontal and vertical scales. Picking of the arrivals from adjacent shots was displayed with thin lines during the interpretation to guide the first-arrival picking for each shot and improve the coherency of layer interpretation at each profile. The interpretation of *P*- and *S*-wave refraction data was done using a commercial software employing the generalized reciprocal method (GRM; Palmer, 1980, 1981) combined with the intercept-slope method for the stations which did not have available reciprocal times.

The tomographic approach for interpreting the profiles was also considered, as these methods provide more accurate results when lithological lateral variations are present, as in the study area. However, tomographic methods often fail to detect sharp vertical velocity changes (Turesson, 2007). In the study area, we have a typical layered sedimentary geological environment where sharp vertical contrasts in velocity are anticipated in a vast part of the study area such as the alluvium/Miocene or Pliocene substratum, or the presence of limestone beds inside Miocene formations. Velocity gradients with depth are also expected for large thicknesses of Cenozoic formations in the

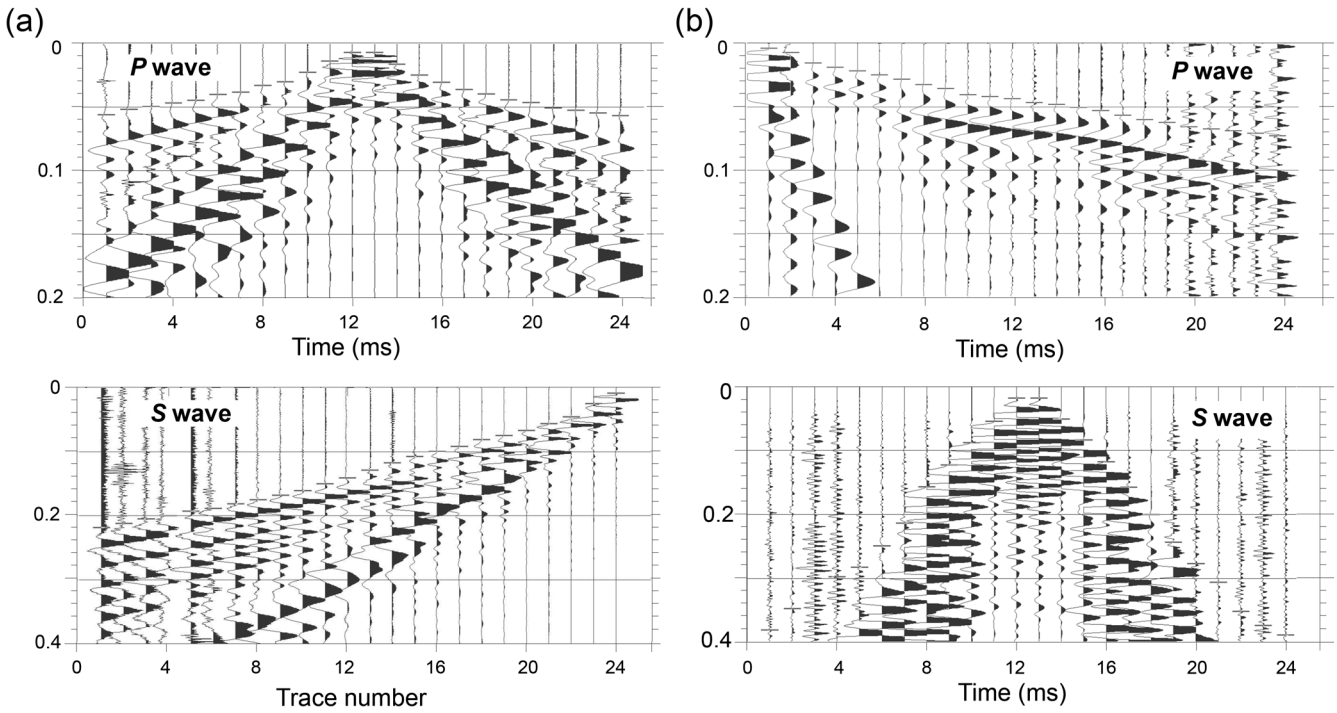

Figure 3. Examples of *P*-wave (top) and *S*-wave (bottom) raw shot gathers for profiles (a) PO18) and (b) TOJ1 (see data in Table A1 and location in Fig. 2). To improve first-arrival picking, records were band-pass filtered and then displayed in varying horizontal/vertical scales. First arrivals are marked by horizontal lines.

study area (the typical vertical velocity gradient in Cenozoic formations according to borehole data is about 1 m/s; e.g., Carvalho *et al.*, 2005), but due to the small investigation depth required in this work, no significant vertical gradients are expected and a layered-earth approach to interpret our dataset appears to be the best. Velocity inversions, a possible major shortcoming of the refraction method if not properly addressed (e.g., Northwood, 1967; Palmer, 1980, 1981; Dobrin and Savitt, 1989; Lankston, 1989, 1990) are relatively uncommon in the study area at the depths required in this work, according to borehole data. This problem was anticipated for seven of the profiles (about 8% of the profiles, see discussion later in this section) and, for the latter, borehole data were used to constrain the depth to the refractors.

First, the travel-time-distance curves were interpreted in terms of layers. At this step, the use of left and right strikes for the *S*-wave source was an advantage in guiding the first-arrival picking, and helped evaluate the number of layers contained in the data. After interpretation of the layers, the reciprocal times were calculated and an inversion was performed using the slopes of the travel-time curves, offering the starting initial velocities. After this, a decision had to be taken if, for each refractor, the slope-intercept method was to be applied for points where reciprocal times were not available or if an interpolation between the GRM interpreted stations was to be made.

Models with different numbers of layers were tested. The root mean square (rms) error for the final model, obtained from integrated interpretation of seismic, borehole, and geological outcrop data, was then calculated. The rms error between the observed and the computed travel times was generally less than 1.5 ms. In Figure 4, we show examples of final interpretations of *P*- and *S*-wave profiles at two different sites: CAR7 (Fig. 4a) and BO20 (Fig. 4b). In the upper part of each figure, the time–distance curves with layer interpretation are shown, while in the lower part the obtained velocity model is displayed. In Figure 4c, we show raytracing performed for *S*-wave model of Figure 4b (Zelt and Smith, 1992). Velocity, depth, geological formation where each profile was acquired according to the 1: 50 K scale geological maps, and other information about these profiles can also be found at Table A1 (ID = 69 and 38, respectively).

To check the geophysical interpretation, we used data from all available nearby (< 1.5 km) boreholes. In the study region, we had available information from thousands of boreholes drilled for water supply and geotechnical studies—covering almost all geological formations in the area. The LNEG is the repository for borehole data in Portugal, and therefore, geological cores, geophysical logs, and SPT data reports could be used free of cost. All this information was collected, georeferenced, and integrated in a Geographic Information Systems (GIS) together with other geological and geophysical data. The boreholes used in the scope of this work reached an investigation depth that varied from 27 m to a few hundred meters, with an average of about 50 m. Not only was the closest borehole to the seismic profile used, but also multiple other available boreholes in the area were utilized, which gave us a better idea of the geology of the region around each profile, in particular of possible lateral variations

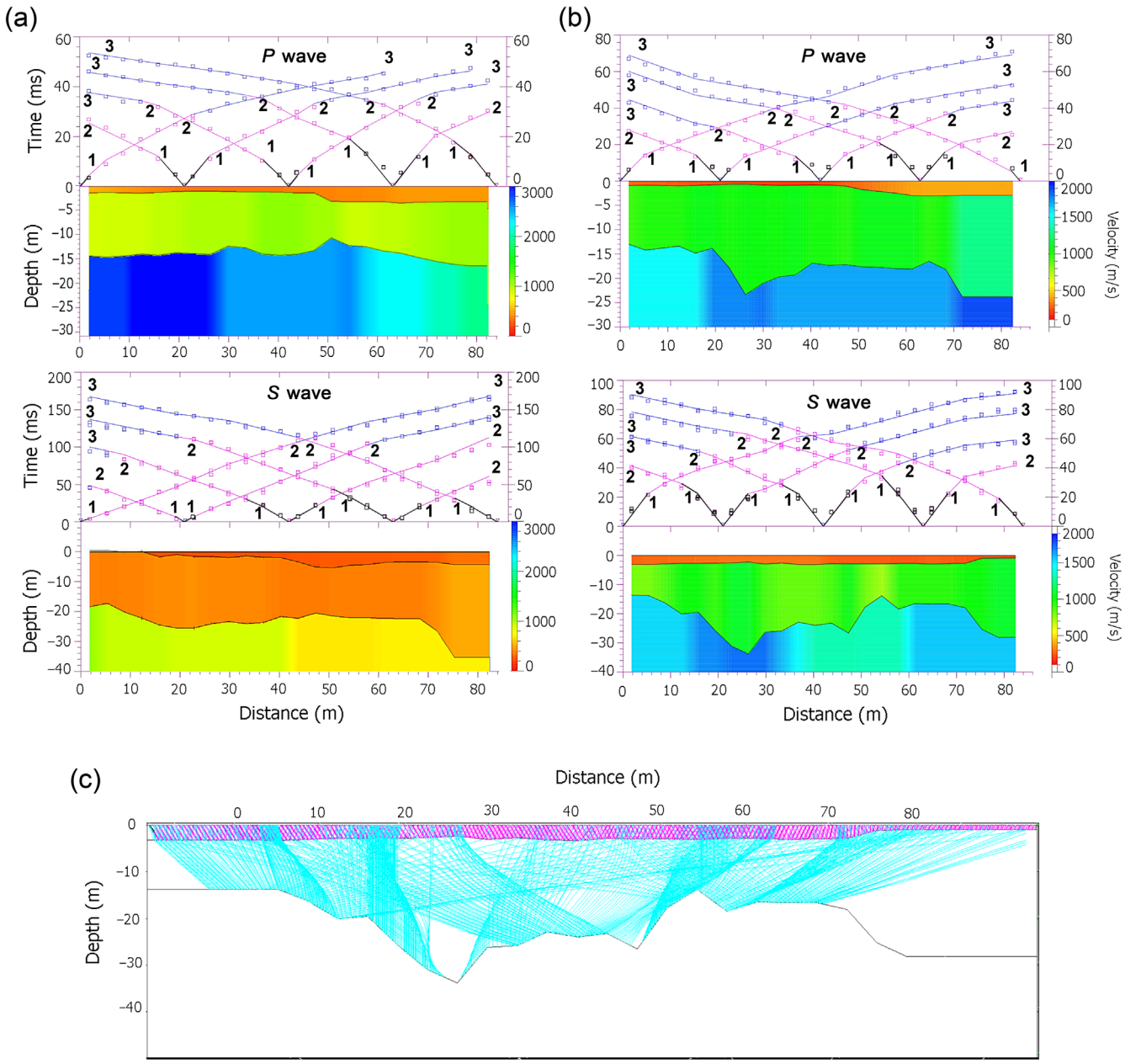

Figure 4. Examples of velocity models derived from the interpretation of *P*- and *S*-wave seismic refraction profiles, located in (a) CAR7 and (b) BO20 (see location in Fig. 2). Top panels display time–distance curves with layer interpretation (numbers indicate approximate location of the furthest receiver from the source registering arrival from the *i*th layer). Squares indicate arrival times at each receiver. The bottom panels show the derived velocity models. (c) Raytracing (Zelt and Smith, 1992) for the *S*-wave model of profile BO20 (b) showing that for typical velocity distributions in the region, the receiver spread length used in this work is capable of recording arrivals from seismic interfaces close to 30 m depth. The color version of this figure is available only in the electronic edition.

in layer thicknesses and lithologies. For some profiles, more than 10 boreholes were used in the interpretation but, on an average, 3 boreholes per profile were used in the interpretation. Only for profiles VER2, CRA27, and ALC19 (see Table A1, ID = 51, 45, 56) borehole data not used. Additionally, we carried out a detailed geological survey at each profile site to avoid missing any possible lateral lithological variations undetected by borehole data and ensure an adequate lithological control at each profile location.

Inside each seismic layer, lateral velocity variations in most of the profiles varied between 4% and 34%, but in some cases, as in the example of profile CAR7 shown in Figure 4, or profile A10, velocity variations went up to 49%. On an average, these velocity variations are about 25% and are due to lateral lithological changes along the 84 m long profile, observed either in the geological outcrop surveys or borehole data. Nevertheless, interfacial irregularity observed in some profiles might have been enhanced due to the depth interpre-

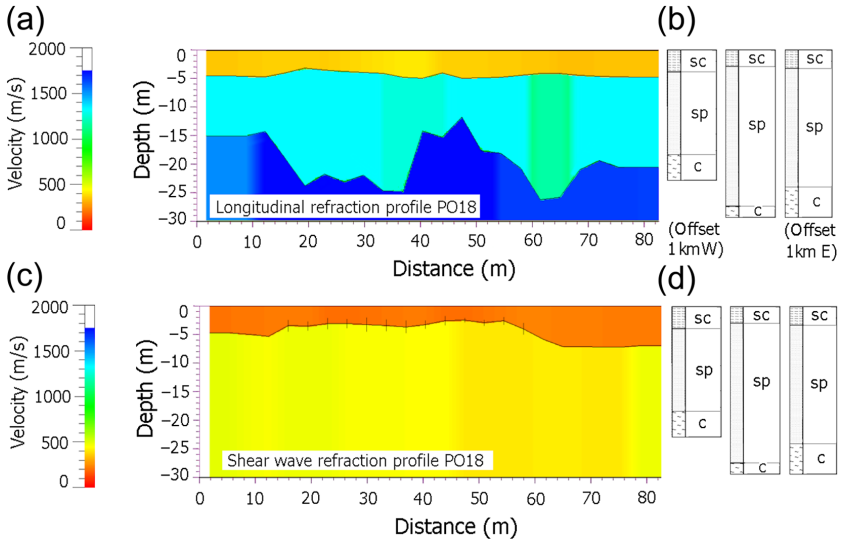

Figure 5. (a) V_P model for seismic refraction profile PO18, acquired over fluvial terrace deposits formation of the Pleistocene. (b) Boreholes used in the interpretation: Sc, sandy clay; sp, sand with pebbles; c, clay. (c) V_S model. (d) Boreholes (repeated from b). A deeper clay layer was detected only in the V_P model due to differences in physical properties that affect *P*- and *S*-wave velocities. The color version of this figure is available only in the electronic edition.

tation errors such as the first-arrival picking errors or incorrect layer assignments (e.g., Northwood, 1967; Kilty *et al.* 1986; Dobrin and Savitt, 1989). The first type of error introduces depth errors that are proportional to the time-picking error and increases as the contrast of velocities above and below the interface diminishes, or the average velocity to the interface increases (Northwood, 1967). To avoid this type of errors, we used a decent sampling of the surficial velocities (five shot points per profile) and discarded any arrival time that was unclear. For arrivals with a clear break, a picking error of ± 3 ms is assumed. Using the approach of Kilty *et al.* (1986) and the typical velocities obtained in our data, a depth error of less than 2 m is expected. Errors resulting from recognizing an incorrect number of layers present in the time–distance curves will also generate errors in the refractor velocity estimation due to incorrect slope calculation, which will, in turn, introduce depth errors, which will increase with refractor dip and average velocity to the refractor. The effect of lateral velocity changes due to lithological variations will produce similar bias to the travel-time curves and consequent velocity and depth errors. Borehole and geological outcrop data often helped us detect these lateral lithological changes and interpret the time–distance curves. The generalized reciprocal method is also well suited to address lateral velocity changes, either in the refractor or overburden (Palmer, 1981).

Incorrect assumption errors such as velocity inversions or the hidden layer problem (e.g., Palmer, 1981) are more difficult to estimate. Each profile was interpreted taking into consideration these limitations of the refraction method, using for this purpose borehole and lithostratigraphic information from the detailed geological surveys. Figure 5 shows another example of *S*-wave velocity model (profile PO18) and the nearby borehole data used in its interpretation. In this example, the borehole data and the geological survey carried out in the area show that there is a clay layer beneath the predominantly sandy outcrops of the fluvial terrace deposits, at depths varying from 15 to 28 m. This clay layer was not detected in the *S*-wave model, but *P*-wave data interpretation clearly shows the presence of a higher velocity layer at depths varying approximately between 15 and 25 m. We attribute this discrepancy in the *P*-wave and *S*-wave models to the distinct physical properties that the two types of seismic waves respond to. While *P*-wave velocity is slightly higher than *S*-wave velocity for clays than for medium-to-coarse-grain wet sands (according to borehole data, the water table in this area is around 5–8 m deep), *S*-wave velocity may be lower in clays (e.g., Bourbie *et al.*, 1988), and therefore, may correspond to a velocity inversion, which would not be detected in the *S*-wave refraction data.

Borehole data along with detailed geological surveys were used to check if the required investigation depth (30 m) had been reached in the refraction profiles. No significant lithological changes, high-velocity lithologies, or highly compacted layers were found in the boreholes between the deepest seismic interface detected in each refraction profile and a depth of 30 m. This shows that no undetected velocity changes are present above a depth of 30 m, and therefore, the 84 m refraction spread was long enough to achieve the required investigation depth, or that at least, no important velocity changes are found until a depth of 30 m. Furthermore, Table A1 shows that several seismic interfaces have indeed been detected close to 30 m depth, and on a few occasions, below 30 m. In the raytracing performed for profile BO20, it can be seen that with a typical velocity distribution in the region, the critical rays from the deepest seismic interface close to 30 m depth are detected with the receiver spread length used in this work.

Using jointly seismic refraction, geological surveys, and borehole data, we were able to derive an appropriate relationship between seismic velocity and geological formation, lithology, age, and the depth of burial. Information regarding the water table depth was also collected, whenever possible. Depth of water in the nearby water bodies (rivers, creeks, dams, lakes, water wells, etc.) was checked at the time of acquisition of the seismic profiles. General information about water table depth in the LTV region can also be found, for example, in Simões (1998, fig. 4.9). The borehole and geological information was only used in the second phase of interpretation. We generally started the interpretation using the *S*-wave data due to data redundancy (strikes from opposite sides of the seismic source). A third round of interpretation was carried out to ensure, as much as possible, the

Table 1
Average Depths (to Top of the Second Layer) and Measured V_S of the Second Layer, for All the Refraction Data Points Collected in This Work, Organized by Age and Main Lithologies, Provided That the Thickness of the First Layer Is Less Than 2 m (See the Deriving V_{S30} and Soil Classification Maps section)

Age	Main Lithologies	Average V_S (m/s)	Average Depth to Top of Layer (m)	Number of Data Points	Standard Deviation (m/s)
Holocene	Clays	346	8	19	162
Holocene	Sands and gravel	366	3	5	144
Pleistocene	Sands and gravel	484	8	16	243
Pleistocene	Sands andmarls	372	8	1	—
Pliocene	Sandstones	543	7	10	196
Miocene	Carbonate sandstones and claystones	556	2	16	333
Miocene	Sandstones and claystones	536	5	6	260
Cretaceous	Weathered basalts	560	2	2	60
Jurassic	Sandstones and limestones	1077	1	1	—
Jurassic	Sandstones and claystones	536	7	1	—
Precambrian	Gneisses	1240	1	1	—

consistency between *P*- and *S*-wave velocity models. Generally, models with two or three layers until the depth of interest (30 m) were obtained. In Table 1, we present an averaging by age and lithologies of the *S*-wave velocities measured in the study region.

Use of Old *P*-Wave Refraction, SPT, and Crosshole Datasets

In 1997, 49 *P*-wave refraction profiles were acquired for a seismic hazard assessment project in the LTV region. Some of the profiles acquired in the present research are located close to these profiles of 1997 and are in the same geological formations. We revisited the locations of the old *P*-wave profiles to investigate which of them were positioned over the same lithologies as those acquired and processed in this study. For the cases for which the refraction profiles were located over the same geological formation and lithology as the old profiles and an investigation depth of 30 m or more could be derived, we made use of the V_P/V_S ratio found in the current profiles and applied it to estimate *S*-wave velocities at the old *P*-wave survey locations.

In addition, SPT values that were collected at the old *P*-wave refraction profiles at 1 or 2 m depth interval were used where available, to correlate the interpreted seismic refractions with velocities and geological data (and detect the eventual presence of velocity inversions), and to check if the required investigation depth of 30 m was reached. SPT is a tool traditionally used in geotechnical engineering to assess the compaction of soils or sediments. A metallic tube is driven into the ground at the bottom of a borehole by hitting the tube with a hammer. The sample tube is driven 150 mm into the ground and then the number of blows needed for the tube to penetrate each 15 cm up to a depth of 45 cm is recorded. The sum of the number of blows required for the second and third penetration of 15 cm is termed the standard penetration resistance or the *N*-value (N_{SPT}). For example, if a very compacted layer was detected in SPT but the refraction model did not present a high-velocity layer at this approximate depth, then we considered that the refraction profile was not usable in calculating the V_{S30}. To ensure that the estimation of V_S from these old *P*-wave datasets was adequate, we used only an old profile that presented a similar velocity model to a nearby refraction profile acquired recently (2011–2013 survey) over the same lithology. N_{SPT} was also used, wherever available, to check if velocity inversions or thin layers undetected by the refraction method were present.

Another possibility to obtain V_S from these old *P*-wave profiles was to use V_P/V_S ratio or Poisson ratio available in the literature for similar geological formations. The Brocher's regression fit that was derived for rock and sediment samples from the United States (Brocher, 2005), and from which V_S can be obtained from V_P, was used here for comparison. However, Brocher's regression fit is valid for $1.5 < V_P < 8$ km/s, and therefore, unsuitable for many of the velocities obtained in this research. In the V_P validity range of Brocher's regression fit, high V_P/V_S ratios and low V_S estimates were obtained for the old *P*-wave data used in this work. For example, for profile PS1, a V_S of 1240 m/s is obtained for weathered gneisses with a *P*-wave velocity of 1630 m/s using the approach above, while using Brocher's regression fit, a value of about 400 m/s is estimated. Occasionally, for a few profiles such as profile PS10, located close to profile PO18, higher estimates of V_S using our approach (204 m/s) are obtained than using Brocher's regression fit (375 m/s), resulting in unrealistic V_P/V_S ratio < 1. This is probably due to the larger investigation depths used to obtain Brocher's regression fit or other relationships found in the literature (e.g., Castagna *et al.*, 1985).

If we use V_P/V_S ratios available in the literature for dry and saturated unconsolidated sediments (e.g., Lankston, 1990) such as alluvial clays (V_P/V_S equal to 1.78 and 4.35, respectively) or quaternary sands and gravels (V_P/V_S equal to 2.03 and 4.09, respectively), we get V_S values that vary by less than 70% compared with those obtained using the approach adopted here. The latter, which considers only V_P/V_S ratios from recent profiles acquired close to or

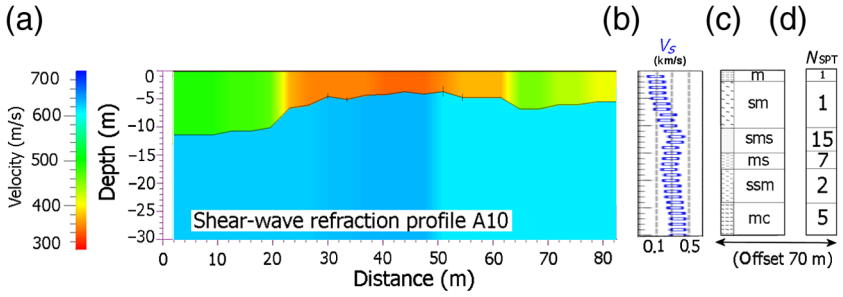

Figure 6. (a) V_S model from the refraction profile A10, carried out over alluvium. (b) Nearby crosshole velocity information. (c) Borehole geological log. m, mud; sm, sandy mud; sms, slightly muddy sand; ms, muddy sand; ssm, slightly sandy mud; mc, muddy clay. (d) Standard penetration test (SPT) data. N_{SPT}, N parameter. The color version of this figure is available only in the electronic edition.

over the same lithologies as the old ones and that possesses a similar velocity model, seems more robust as it uses local lithological information and does not require water depth information for each profile.

Using this strategy, we were able to add 36 data points to our dataset. There were 13 old *P*-wave refraction profiles that could not be used, either because although they were acquired over the same geological formation as a nearby recent refraction survey, the lithology was different, or because according to boreholes and the detailed geological survey, these profiles probably did not reach the required investigation depth of 30 m. Figure 2 also shows the location of the 36 old profiles that could be used.

In addition, we made use of two crosshole V_S measurements in the Benavente area, which were carried out for an engineering construction, and three geotechnical boreholes acquired in the downtown Lisbon, increasing the total number of V_S measurements in the Lower Tagus region used in this work to 82. The velocities determined from the crosshole measurements are shown in Figure 6. The downtown Lisbon borehole measurements have been discussed in Teves-Costa *et al.* (2014), who estimated V_S from the N_{SPT} using empirical relationships that were calibrated by ambient vibration (AV) analysis (horizontal-to-vertical [H/V] curves—H/V spectral amplitude ratio [HVSR] of an AV measurement). We used the V_S published by these authors to estimate approximate V_{S30} and soil types in three locations in downtown Lisbon—at north, center, and south. The V_S values range between 175 and 240 m/s, and the soil classes are C and D.

Velocity Model Results

All shear-wave velocities determined and used in this research are presented in Table A1, organized in geological units. The measured *P*-wave velocity varies from about 130 to 1140 m/s and from 430 to 2500 m/s in the first and the second layer, respectively. The estimated V_S ranges are approximately 60–690 m/s and 140–1650 ms/s for the first and second layers, respectively.

For the first layer, V_P/V_S ratio exhibits a range from 0.60 to 6.07. If we calculate Poisson's ratio (ν) using the empirical formula (e.g., Christensen, 1996; Brocher, 2005)

$$\nu = \frac{1}{2}\{1 - 1/[(V_P/V_S)^2 - 1]\}, \qquad (1)$$

we obtain a variation of ν from negative values to values above 0.50. Typical values for V_P/V_S ratio found in shallow, dry unconsolidated sediments, compacted sediments and igneous/metamorphic rocks range 1.77–2.02, 1.46–1.97, and 1.49–2.08, respectively (e.g., in Lankston, 1990). Pickering (1970) has shown theoretically that ν-values vary between −1 and 0.5. Negative values of ν have long been associated with the presence of air or gas (Gregory, 1976). Saturated, unconsolidated sediments (with high porosity) present values close to 0.5 (Stuempel *et al.*, 1984). Coarse-grained, hard materials such as compacted coarse sands and gravels present low V_P/V_S ratio and ν, while soft, fine-grained materials possess higher ν (Tatham, 1982).

The unrealistic low values of V_P/V_S and negative ν for the first layer obtained in this work can, therefore, be explained by the likely presence of air, organic matter, and other materials (e.g., Gregory, 1976; Konstantaki *et al.*, 2016). As explained above, these low values usually occur when the first layer is less than 2 m thick, and in that case, according to borehole data its lithology/geology is not representative of the geology indicated in the geological maps. For example, one may have a sandy top soil of 1 m thickness with significant rubble content in a region where the Miocene clays generally outcrop. Furthermore, errors in the estimated velocity due to limited number of receivers used in recording the direct arrivals may have also contributed to such abnormal V_P/V_S values. In the second layer, V_P/V_S and Poisson ratio range from 1.48 to 7.46 and from 0.11 to 0.49, respectively (discussed further at the end of this section).

P- and *S*-wave velocity models in many refraction profiles are similar in number and depth of the layers, but in some profiles the depths are substantially different. Where the water table is shallow, V_P increases greatly with water saturation (contrary to V_S), and the refraction method does not allow the detection of deeper layers unless a very high-velocity layer is present, which rarely happens at the maximum investigation depths that are reached. This can explain the observed discrepancy at most sites between the depths resulting from V_P and V_S models. When the water table is very shallow, the profiles present the highest V_P/V_S ratio and highest ν for the seismic layers beneath the water table, due to an increase in the *P*-wave velocity with water content. For other profiles, the discrepancy in interface depth between *P*- and *S*-wave velocity models can be attributed to different properties that are addressed by these two wave types.

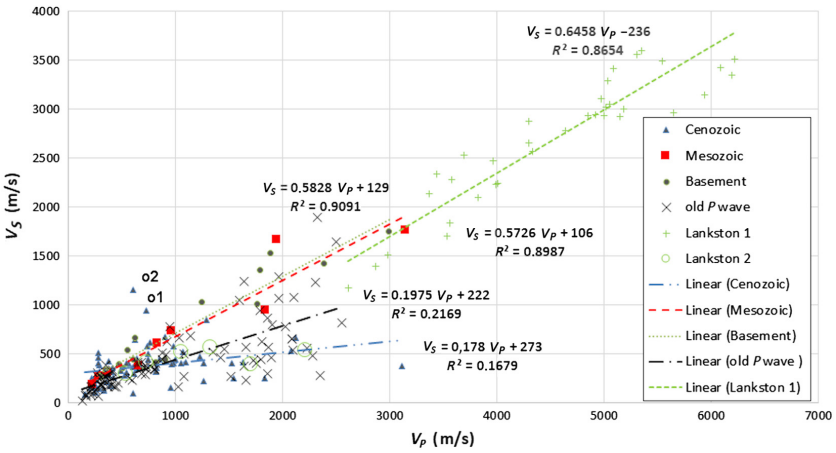

Figure 7. Plot of V_S versus V_P for the sediments and rocks of the study area. For each refraction profile, every velocity layer is represented by a data point. The data have been divided into distinct chrono-lithological groups: (1) Cenozoic sedimentary units, (2) Mesozoic sedimentary formations, (3) igneous or metamorphic rocks of Cretaceous to Precambrian, (4) old *P*-wave profiles (all formations), (5) consolidated sediments and rocks after Lankston (1990; Lankston 1) and 6) unconsolidated sediments after Lankston (1990; Lankston 2). Data from the basement include several profiles from outside the study area, not used in this work other than here. The best fit of each data series is shown, together with respective *R*-squared value. o2 and o1: profiles with very low V_P/V_S discussed in the Velocity Model Results section. The color version of this figure is available only in the electronic edition.

In a few refraction profiles such as of BO20, EN21, CCP11, and SET14 (IDs = 38, 39, 48, and 52 in Table A1), *P*- and *S*-wave velocities are unrealistically similar, giving a V_P/V_S of around 1. Refraction profiles BO20 and EN21 were acquired over Pleistocene fluvial terrace deposits formation, whereas profiles CCP11 and SET14 were performed over Pliocene sandstones of the Ulme Formation. Interestingly, all these sites exhibit at the surface very compacted, hard sandstones with high-to-medium concentration of gravels that vary laterally and vertically. Though minor velocity errors (less than 10%) may be present in these profiles, we attribute the estimated low V_P/V_S to the physical properties of these special sites, characterized not only by hard, compacted sediments but also by high anisotropy due to variation in the density and orientation of the pebbles/gravels (e.g., Ghose and Osada, 1993; Salem, 2000b; Essien *et al.*, 2014).

The estimated V_P/V_S and ν-values for all profiles are consistent with those found earlier for similar shallow sediments using seismic refraction data (e.g., Lankston, 1990; Salem, 2000a,b; Uyanik, 2010; Essien *et al.*, 2014). In profiles VFX5, PAN46, and PSE49—all acquired over alluvium sediments where the water table is very shallow (1 m)—we estimated for the second layer much higher V_P/V_S values than those usually found for partially saturated or dry shallow sediments (Lankston, 1990; Salem, 2000a). However, such high values (up to 9) for V_P/V_S have been reported earlier for water-saturated, unconsolidated, or clayey sediments (e.g., Salem, 2000a).

Figure 7 show a plot of V_P versus V_S for all the refraction profiles acquired in this study, and also for the old *P*-wave profiles from which V_S was derived following the methodology explained in the Use of Old *P*-Wave Refraction, SPT, and Crosshole Datasets section. Each layer of the refraction interpretation is represented in the plot of Figure 7 as a sample, and the data have been separated into distinct groups: (a) sedimentary Cenozoic formations, (b) Mesozoic sedimentary formations, (c) igneous and metamorphic rocks from Cretaceous to Precambrian (basement), (d) all rock/sediments types for the old *P*-wave data, (e) V_P and V_S values for consolidated rocks and sediments after Lankston (1990), and (f) V_P and V_S values for unconsolidated sediments (Lankston, 1990). Because of the fact that we had only one profile sampling the metamorphic and igneous rocks of pre-Mesozoic in the study area, we used six other refraction profiles acquired with the same geometry close to the study area over basement rocks.

A few outliers observed in the graphic (Fig. 7) correspond to the above-mentioned profiles with very low V_P/V_S and acquired over hard sandstones with pebbles such as CCP11 and EN21 (labeled o1 and o2, respectively). One can observe that in spite of some scatter in the data there is a clear increase of V_S with V_P for all data series and that this increase is larger for basement and Mesozoic units. We can also see that the V_S derived from the old *P*-wave profile obeys a V_S versus V_P relationship similar to the rest of the profiles. Figure 7 further shows that velocities estimated in this work conform to values calculated by other authors, for example, Lankston (1990), both for consolidated sediments and rocks (series Lankston 1) and unconsolidated sediments (series Lanskston 2).

Deriving V_{S30} and Soil Classification Maps

To calculate V_{S30} values at each measurement site, we used the formula of Borcherdt (1994) for a layered earth

$$V_{S30} = \sum_{i=1}^{n} di / \sum_{i=1}^{n} di/V_{Si}, \qquad (2)$$

in which di is the layer thickness and V_{Si} stands for V_S in the same ith layer. Given that velocity varies along a profile, an average velocity for each layer was calculated from the velocity estimated at each receiver. To supplement the seismic refraction information and the number of data points (velocity measurements), we further utilized the crosshole data in the Benavente area and the information from Teves-Costa *et al.* (2014) for the alluvium cover of the city of Lisbon to produce the V_{S30} and soil classification maps.

To obtain soil classification and V_{S30} maps of the study region, we had to extend and generalize the sparse data

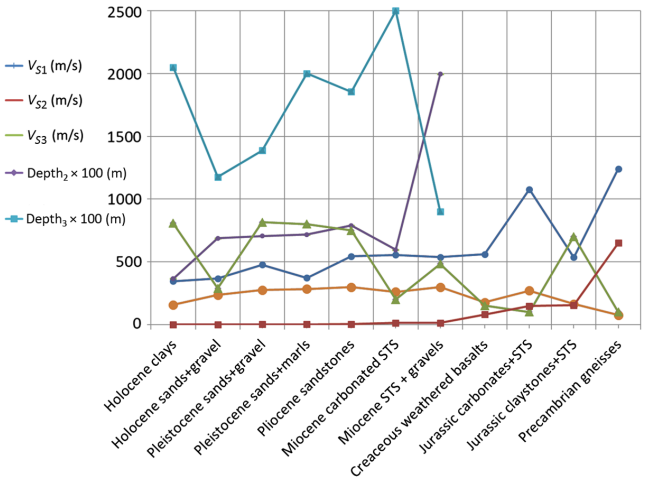

Figure 8. Plot of V_S obtained from interpretation of seismic refraction data considering depth of burial, age, and lithology for all interpreted layers. V_{Si}, velocity of layer i in m/s; Depth$_i$ × 100, depth to top of layer i in meters, multiplied by 100; STS, sandstones. The color version of this figure is available only in the electronic edition.

points providing seismic information (V_{S30} and soil type) to the geological digital maps. This generalization is usually performed using either a geological–lithological approach (e.g., Fumal and Tinsley, 1985; Wills *et al.*, 2000, 2015; Kalkan *et al.*, 2010; Motazedian *et al.*, 2011), a statistical analysis, or the topographic slope method (Wald and Allen, 2007). Our study area incorporates a vast region of flat agricultural plains where we found significant variations in V_S, and therefore, the topographic slope method is not adequate. A statistical approach using the dataset acquired in this work is presented by Vilanova *et al.* (2018). Here, we opted for the use of a geologically lithologically based approach utilizing updated geological mapping and geological–lithological data collected in this work.

To this end, we sampled all post-Paleogene geological formations in the study region. Paleogene formations, which according to velocity information gathered from regions of the world should present a very low seismic risk (e.g., Matsuoka *et al.*, 2005; Perrin *et al.*, 2015), were not sampled. However, a few Jurassic and Cretaceous igneous and sedimentary formations, together with a Paleozoic metamorphic formation, were sampled to check if the weathered layer could present low V_S values, as defined in the Eurocode 8. Though we sampled in our study all post-Paleogene geological formations mapped at the 1:50 K scale, not all geographically distinct outcrops of a particular geological unit were sampled.

To understand the sensitivity of our velocity/depth data and the validity of the data generalization process, we analyzed our dataset, organizing it by considering three important factors that control the seismic body-wave velocities: age, lithology, and depth of burial. This compilation is shown in Table 1 and in Figure 8 in graphical form. Table 1 presents only the velocity and the depth to the top of the second layer (when the surficial layer is < 2 m thick), as the first layer is often a thin uncompacted surficial soil layer containing gas and organic materials, as already discussed, and is not representative of the lithology sampled. Figure 8 shows also velocity for the first and third layers, and depth to the top of the third layer. The third layer is not always present, as its lithology is sometimes not adequately constrained by the detailed geological surveys or by borehole data. However, for the calculation of V_{S30} and the soil classification maps, the velocity/depth information in the first and the third layer were, of course, taken into consideration.

Figure 8 and Table 1 illustrate that it is possible to separate some of the sedimentary and igneous geological formations using V_S information acquired in the study region. For example, a sharp increase in velocity is observed with age for the pre-Cretaceous formations or Precambrian gneisses. Sedimentary Cenozoic formations present an average velocity of about 405 m/s, whereas the former has an average velocity of 855 m/s. In addition, although the main lithology of the sediments (e.g., dry clays and sand) exhibits overlapping velocities (346–372 m/s), the presence of carbonates is clear in this dataset, indicated by a sharp rise in velocity (to ~546 m/s), independent of age or depth of burial. It is interesting to note that the Jurassic sediments (sandstones and claystones) present average *S*-wave velocities (536 m/s) that are identical to those found for similar lithologies of the Miocene, probably due to strong weathering. This will be discussed later on.

Other sedimentary formations (sands, sandstones, and claystones) shown in Table 1 have overlapping V_S values, as expected for these lithologies, irrespective of the age (Miocene or Pliocene), but the average velocity values are distinctive for some of these formations. *S*-wave velocity depends not only on lithology but also on age, depth of burial, cementation, water saturation, grain size, etc. At the shallow investigation depths addressed in this study, the depth of burial seems to be the least important factor affecting velocities.

In this work, velocity variation with depth for Holocene and Pleistocene formations using a second-order polynomial regression which obeys the relation:

$$V_S = 0.2142 + 31.949z - 671.87z^2, \tag{3}$$

in which V_S represents the *S*-wave velocity in kilometer per second and z the depth in kilometer. For older Cenozoic formations, the following relation was encountered:

$$V_S = 0.218 + 63.13z - 1502.9z^2. \tag{4}$$

In both cases, average velocities and depths were used, and equations (3) and (4) are valid for the investigations depths reached in this study (up to ~40 m). Brocher (2008) performed a study for velocity variations with depth in northern California until a depth of about 40 m for similar ages and lithologies using vertical seismic profile data, and obtained the following equations for Holocene/Plio-Pleistocene and older Cenozoic rocks, respectively

Table 2

Average V_{S30} Values and Respective Standard Deviations for the Geological Formations of the Study Area (at the 1:50 K Scale) That Have More Than 1 Data Point, Using Data Presented in Table A1

Geological Formation	Main Lithologies	Age	Average V_{S30} (m/s)	Standard Deviation (m/s)	Number Data Points
Alluvium	Clays, sands	Holocene	280	120	24
Undifferentiated sands and gravels	Sands, gravels	Holocene/Pleistocene	464	172	6
Fluvial terrace deposits	Sands, gravel	Pleistocene	452	151	14
Ulme Formation	Sandstones	Pliocene	486	140	11
Lisbon, Miocene: Banco Real Formation, Musgueira Limestones, etc.	Limestones, sandstones, claystones often with carbonate crusts	Miocene	700	313	11
Alcoentre Formation and Tomar Clays Formation	Sandstones, claystones often with carbonate crusts	Miocene	435	179	11
Basement	Varied	Pre-Cenozoic	780	280	5

Basement includes metamorphic and igneous formations of Cretaceous to Precambrian. For full description of Lisbon Miocene formations, see Geological Setting section. The basement presents a lower average value and high standard deviation due to the abnormal value for the Jurassic sandstones of Abadia Formation (profile PS43, see Table A1), possibly due to weathering.

$$V_S = 0.215 + 10.932z - 138.1z^2, \quad (5)$$

$$V_S = 0.215 + 18.3z - 138.1z^2, \quad (6)$$

which provide lower V_S values at the same depth compared to the ones derived for the study area. For example, at a depth of 10 m we obtain a V_S of 310 m/s in California for Holocene and Plio-Pleistocene formations, whereas at the LTV a V_S of 466 m/s is obtained for Holocene and Pleistocene formations. The higher V_S values obtained for the LTV, which bias the regression, are due to the fact that the profiles were acquired over very hardened Pleistocene gravels (e.g., in profiles PS20, BO20, and EN21; see entries 28, 38, and 39 of Table A1), whereas in California the equivalent Plio-Pleistocene Santa Clara Formation consists of sandstone and gravels that are poorly to moderately indurated. This seems to explain the higher V_S obtained for the LTV region. For Neogene formations in the LTV region, we obtain at a depth of 20 m a V_S of 879 m/s, whereas in California a V_S of 526 m/s is calculated for the older Cenozoic units at the same depth. Hard compacted limestones are very probably the cause for these higher values observed in the LTV, as suggested by the higher V_S values measured in the profiles acquired over the Lisbon Miocene or Alcoentre Formations (e.g., entries 58, 60, and 75 in Table A1).

In Table 2, we present the average V_{S30} values and the respective standard deviation for groups of geological formations in the study area, organized by age (Epoch) as in Figure 2. However, in Table 2 the pre-Miocene geological formations have been grouped into a single unit (basement). V_{S30} values include different lithologies and geological formations, and they do not necessarily individualize near-surface geology or lithology. Taking this into consideration, along with the laterally varying thickness and velocity, one cannot expect that a certain geological formation should represent a single V_{S30} class. The data point acquired over the Porto Carro marls (see Table A1) has been included in fluvial terrace deposits formation due to similar lithology and age. The alluvium, the Miocene formations containing carbonates together with Pliocene units, and the basement have clearly distinctive V_{S30} values, with averages of 356, 545, and 855 m/s, respectively. Pleistocene formations show large variations in velocity but present different average velocities compared with the other formations (484 m/s for sands and gravels, and 372 m/s for sands and marls). Standard deviations shown in Tables 1 and 2 demonstrate that V_S and V_{S30} values for each geological formation have relatively large variations, depending on lithology, layer thicknesses, and other factors such as clay content, water content, grain size, etc., and according to the geographical position within the study area. Together with *a priori* geological information, our database contains enough information to allow the extension/generalization of the data points to the geological polygons, in case appropriate care is taken.

As stated above, to produce the V_{S30} and soil class maps, the sparse seismic data samples were extended/generalized to the geological polygons of 1:1 M scale (LNEG, 2010), using available digital geological cartographic information in a GIS environment. Carvalho *et al.* (2013) plotted 34 V_{S30} color-coded data points over a geological map of the LTV region, demonstrating the challenges in producing V_{S30} and soil classification maps using only geological information. In the present study, we faced two major difficulties. First, as stated above, the lithostratigraphic maps and vectorial digital geological maps at the 1:50 K scale were not available for the entire study area, which made it difficult to generalize a few data points to a particular outcrop of the 1:1 M scale map (hereafter, a geological polygon or polygon) that was used to present our results and where geological formations have been grouped by age (Figs. 2, 9, and 10). Therefore, each polygon might include distinctive geological formation and lithologies. Second, although all post-Paleogene were sampled, not all geographically distinctive outcrops of a

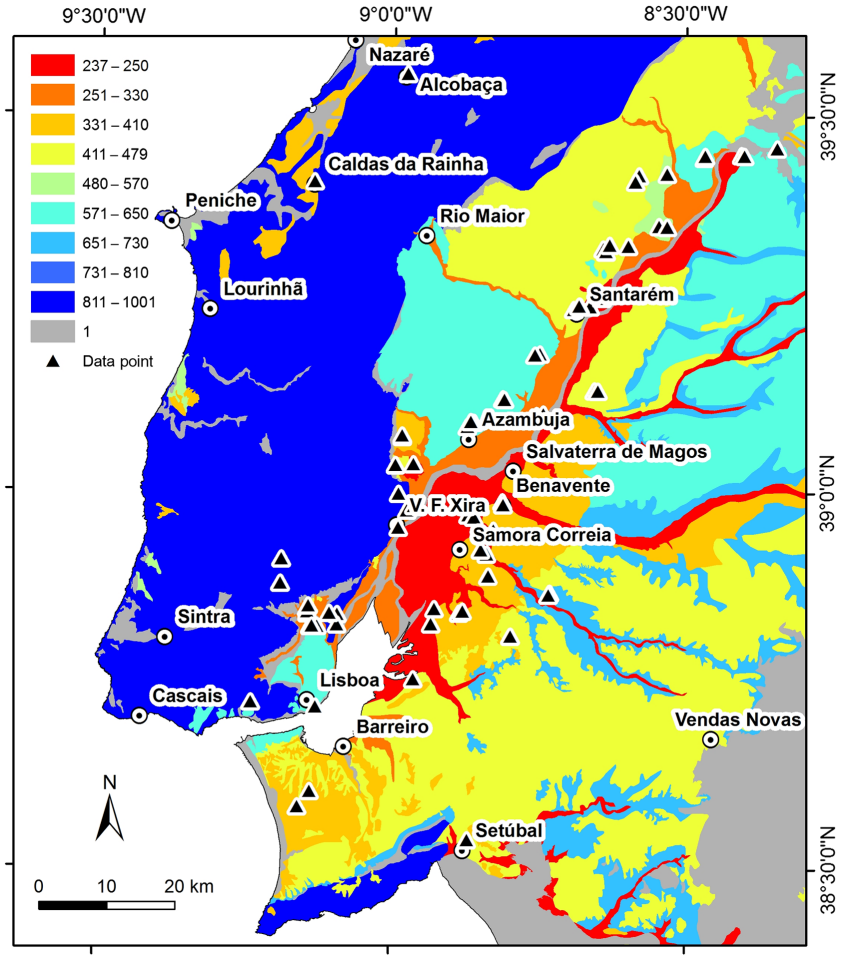

Figure 9. V_{S30} map produced for the study area. Data points (triangles) are generalized/extended to the geological map at 1:1 M scale shown in Figure 2 (LNEG, 2010), using 1:50 K scale geological maps and lithostratigraphic information acquired in this study. 1, areas not sampled in this work. The color version of this figure is available only in the electronic edition.

certain geological formation (corresponding to different geological polygons in Figs. 2, 9, and 10) were sampled.

To address the first problem, we used the digital geological cartographic data in scales from 1:50 K to 1:500 K and the lithostratigraphic information at a fine scale obtained in this work to detail the geological formations and the lithologies within each polygon of the 1:1 M scale geological map. When data points (refraction profiles) inside a particular polygon of our 1:1 M scale map contained a single lithology or geological formation, we simply averaged the V_{S30}/soil-type value/class in that polygon. If several lithologies/geological formations were present inside a polygon, then using the information above (published 1:50 K scale geological maps and geological survey carried out in this work), we calculated an average of the V_{S30}/soil-type value/class weighted by the approximately estimated area occupied by each lithology, as no exact vector mapping of the lithological boundaries exists for the entire study area. For example, if inside a particular geological polygon there were three data points with V_{S30} value 200, 500, and 550 m/s, but the lithology of the refraction profile with $V_{S30} = 200$ m/s occupied approximately half of the area of that particular geological polygon and the other two profile lithologies occupied equally 25% of the area each, then an average V_{S30} value of $363 (= 200 \times 0.5 + 500 \times 0.25 + 550 \times 0.25)$m/s was set for that particular geological polygon.

As mentioned earlier in this section, a second challenge emerged when we found that some outcrops of a particular geological unit (polygon) were not sampled by seismic refraction profiles. In these cases, we averaged a value from the nearest data point (refraction profile) of the same geology and lithology in nearby polygons. If seismic profiles sampling a similar lithology in the nearby polygons were not acquired, then this particular polygon was plotted with gray color. This situation, however, rarely occurred.

Because of these unmapped lateral variations in lithology inside a geological formation and the thickness variations inside a specific lithology, each geological formation was frequently characterized by different V_{S30} classes or soil types. On the contrary, certain lateral velocity and depth changes might also cause the polygons corresponding to different geological formations to belong to the same V_{S30} or soil-type class. Using the approach explained above, we produced the V_{S30} map shown in Figure 9, which corresponds to the geological map at 1:1 M scale (LNEG, 2010).

Next, using the same approach we focused on the construction of the soil classification map. This type of map determines the level of seismic activity to be considered for the design of engineering structures and is useful for mitigating the effects of an earthquake (e.g., Penelis, 1997; Kanlı *et al.*, 2006; Pitilakis *et al.*, 2012, 2015; Sucuoğlu and Akkar, 2014). Soil classification maps together with land occupancy data can also be used to estimate the level of the expected damage and casualty, and to guide the civil protection agencies in their plans of action in case of an earthquake. In these engineering soil classifications, soil conditions are defined using V_S, layer thickness, and N_{SPT} information.

Contrary to the preliminary work carried out by Carvalho *et al.* (2013), in this research we produced a classification based on the Eurocode 8 (2004). The criteria used in this work are shown in Table 3, together with other codes used in the United States (ICBO, 1997; BSSC, 2001). We used additional information based on studies performed by others to complete our soil-type classification map, for example, a few earlier reports used to locate areas where liquefaction

had occurred and S2 type soils were identified (Johnston and Kanter, 1990; Mendes-Victor *et al.*, 1994; Justo and Salwa, 1998; Cabral *et al.*, 2004; Mendes-Victor *et al.*, 2009; Teves-Costa and Batlló, 2011; see later this section).

The obtained soil classification map is presented in Figure 10. Similar to the V_{S30} calculations, the attempted soil classification was highly affected by the geological complexity (lateral changes and layer-thickness variations) in the study region. For the outcrop located in the southeastern corner of the map (Paleozoic terrains), the values of V_S obtained for the Paleozoic gneiss clearly indicate that this region belongs to soil-type class A. This is in spite of the fact that the profile PS1 (see entry 82, Table A1) was acquired over an alluvium cover of about 1 m thickness. Therefore, contrary to the V_{S30} map, where the region is marked as unsampled, a geological polygon is designated in the soil-type map.

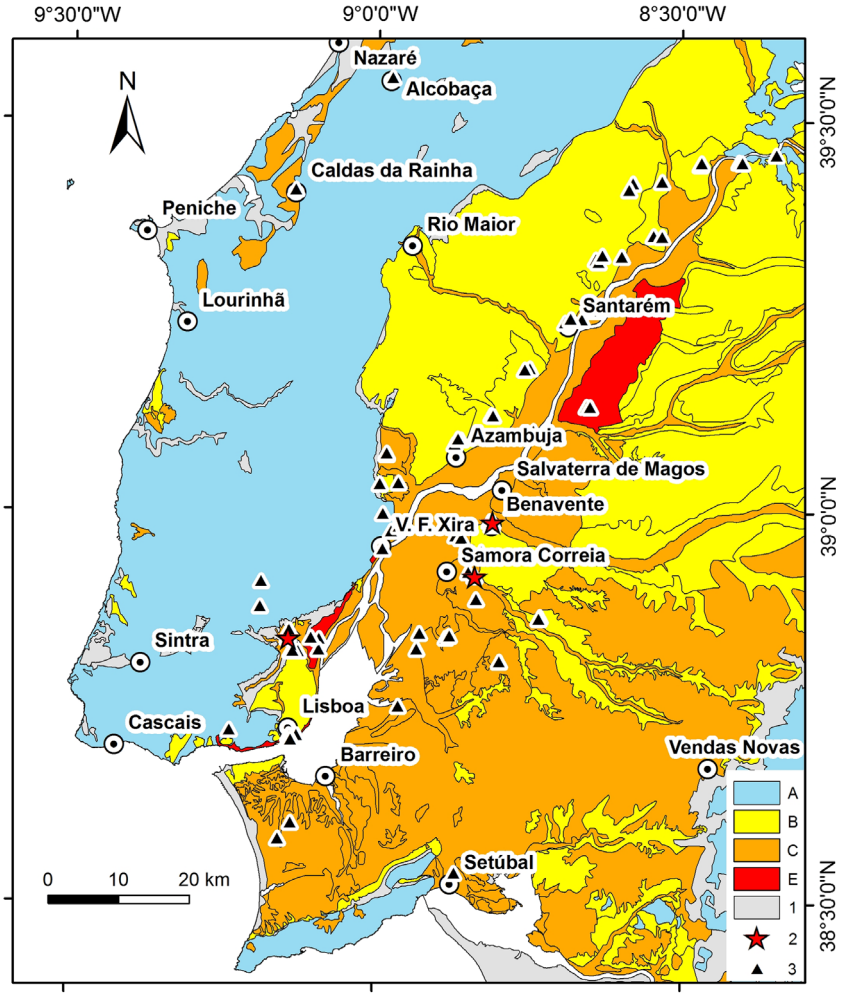

Figure 10. Soil-type map based on the Eurocode 8 (2004) classification. Data points (triangles) are generalized/extended to the geological map at 1:1 M scale shown in Figure 2 (LNEG, 2010), using 1:50 K scale geological maps and lithostratigraphic information acquired in this study. 1, areas not sampled in this work; 2, locations where liquefaction has been historically reported; 3, data points. The color version of this figure is available only in the electronic edition.

Discussion

The maps shown in Figures 9 and 10 highlight the extreme geological complexity in the study region. In this research, we used seismic refraction data to estimate layer thickness and V_S. Nearby borehole data and SPT data, together with detailed geological surveys at each site, helped us overcome major refraction interpretation problem (e.g., velocity inversion) and confirm if the target maximum investigation depth of 30 m was reached. A comparison of refraction results with seismic noise measurements (Appendix B) and crosshole data at several sites validates that the achieved results concerning the estimated average V_S for each geological formation are reasonable. The presence of good lithostratigraphic information is of vital importance to correctly generalize/extend the V_{S30} and soil-type class data, in order to decipher the corresponding polygon representing a certain geological formation.

Unknown depth variations of the different geological formations and the lack of information on the distribution of lithological boundaries probably introduced errors in the V_{S30} map, and hence in the soil-type map. If more data are assimilated in the future, then by using the approach proposed here, more rigorous and detailed maps can be produced. A statistical analysis of the database may also help quantify the uncertainties in these maps (e.g., Vilanova *et al.*, 2018) in the future. For the V_{S30} map presented here, we used V_S classes of 80 m/s. If we assume a maximum error of 20% in seismic velocities and thicknesses, we will get a maximum error in V_{S30} below 80 m/s. We expect that our measurement errors are well below this 20% estimate, so that the velocity classes present in this research prevent errors in the V_{S30} map shown here.

Even in areas of bedrock (Mesozoic and Paleozoic) outcrop, where the weathered layer is thick, resonance effects (the surficial, thick weathered layer producing a strong amplification of seismic waves due to the velocity contrast) may cause the area to fall into soil-type E. An example of this is the value obtained for Jurassic weathered sandstones and limestones (profile PS45, ID = 80 in Table A1), with velocities of 270 and 1080 m/s, respectively, for the first and second layers at a depth of 7 m. Nevertheless, the 1:1 M scale maps presented here represent the first attempt to produce V_{S30} and soil classification maps of the LTV region and have a reasonable accuracy so as to be useful in land planning, civil protection, and seismic hazard assessment purposes.

Table 3

Soil Classification as Defined in Eurocode 8 (EC8) (2004), Uniform Building Code (UBC; International Council of Building Officials [ICBO], 1997), and National Earthquake Hazard Reduction Program (NEHRP; Building Seismic Safety Council [BSSC], 2001) Codes

Ground Type EC8/ UBC/NEHRP	Description of Stratigraphic Profile for EC8	Ground Description for UBC/NEHRP	V_{S30} (m/s) for EC8	V_{S30} (m/s) for UBC/NEHRP	N_{SPT} (blows/ 30 cm) for EC8
$-/S_A/A$	—	Hard rock	> 1500	> 1500	—
$A/S_B/B$	Rock or other rock-like geologic formation, including at most 5 m of weaker material at the surface	Rock	> 800 m/s	760–1500	—
$B/S_C/C$	Deposits of very dense sand, gravel, or very stiff clay, at least several tens of meters in thickness, characterized by a gradual increase in mechanical properties with depth	Very dense soil and soft rock	360–800	360–760	> 50
$C/S_D/D$	Deposits of dense or medium-dense sand, gravel, or very stiff clay, with thickness from several tens to many hundreds of meters	Stiff soil	180–360	180–360	15–50
$D/S_E/E$	Deposits of loose-to-medium cohesionless soil (with or without soft cohesive layers), or of predominantly soft-to-firm cohesive soil	Soft soil/soil with soft clay	< 180	< 180	< 15
$E/S_F/-$	Soil profile consisting of a surface alluvium layer with values of type C or D and thickness varying between about 5 and 20 m, underlain by stiffer material with V_S > 800 m/s	Special soils	—	—	—
$S_1/-/-$	Deposits containing a layer, which is at least 10 m thick, of soft clays/silts with a high plasticity index (PI > 40) and high water content	—	< 100 (indicative)	—	—
$S_2/-/-$	Deposits of liquefiable soils, made of sensitive clays, or other soil profile not included in types A–E or S_1	—	—	—	—

V_S, *S*-wave velocity; N_{SPT}, *N*-value from the standard penetration test.

Little information on V_{S30} maps is available for Portugal. The V_{S30} map presented here is based on more data than those previously published by Carvalho *et al.* (2013) and Teves-Costa *et al.* (2013). Teves-Costa *et al.* (2013) used a gross geology-based extrapolation, whereas in Carvalho *et al.* (2013), the authors were not able to extrapolate the data points due to lack of data. Silva *et al.* (2015, fig. 4) produced V_{S30} maps for Portugal using the geological approach of Wills and Clahan (2006) and the topographic-slope method of Wald and Allen (2007). Data acquired in the present work shows large V_{S30} variations inside the LTV alluvial plains, suggesting that the topographic slope method is not adequate for the LTV region. The V_{S30} map produced by Silva *et al.* (2015) using the approach of Wills and Clahan (2006) shows similar results to the map presented here, but our map shows more detail. This is because the map of Silva *et al.* (2015) was produced for the entire country; it contains less data points in the study area than in this work and it also used V_{S30} values obtained from geological analogs from other sites of the world. The maps presented here show V_{S30} variations inside several geological polygons belonging to a single V_{S30} class of the map of Silva *et al.* (2015) such as in the Miocene and the Quaternary units. Besides providing greater detail, the maps presented here are more accurate compared to the map of Silva *et al.* (2015), due to the use of V_S information.

We can see in the V_{S30} map of Figure 9 that the central area of the study region that surrounds the Tagus River presents the lowest V_{S30} values. This area is covered by Holocene alluvium (compare Fig. 9 with Fig. 2) and the water table is very shallow, around 1 or 2 m. Though the average V_{S30} values range between 237 and 250 m/s, some data points (seismic refraction profiles) present V_{S30} values below 200 m/s and V_S in the first few meters can be as low as about 20 m/s. One may also note that V_{S30} presents lower values on the left bank of the river due to a greater alluvial thickness. The next V_{S30} class, 251–330 m/s, also corresponds to alluvial sediments. Higher values occur when the Miocene or older units are located at relatively shallow depths beneath the alluvium.

The soil type in the area corresponding to these two V_{S30} classes (237–250 and 251–330 m/s) is of type C, but in at least three of these sites liquefaction had been reported after the occurrence of historical earthquakes. This is the case for the Benavente area, where liquefaction was reported after the 1909 Benavente earthquake (Cabral *et al.*, 2004; Teves-Costa and Batlló, 2011), and for other regions as reported during the 1755 and 1531 Lisbon earthquakes (Mendes-Victor *et al.*, 1994; Justo and Salwa, 1998; Mendes-Victor *et al.*, 2009), and the 1858 Setúbal earthquake (Johnston and Kanter, 1990), for example. Though this investigation is still limited, these locations where liquefaction was reported are marked with stars in Figure 10. Although this area where liquefaction occurred was classified with soil-type C based on the V_{S30} values, the area may also be classified as S1 soil type, because according to borehole and trench data, the alluvium soils here are often composed of clays and silts with a high degree of plasticity and water content.

In the present work, the alluvial sediments that surround the central Lisbon city were sampled once by a seismic refraction profile. Only the alluvial sediments slightly north

of the central Lisbon were visited (profile TOJ1). The V_{S30} value found at these sites is about 150 m/s and falls into soil-type S1. The alluvial sediments in central Lisbon close to the Tagus River are also expected to have a high risk, and as stated above, have been the focus of a detailed work in the past (Teves-Costa *et al.*, 2014). V_{S30} values range from 170 to 240 m/s and soil type is class C or class D.

Closer to the Tagus River, the water table is shallower, and we again find S1 or S2 type soils. Other crosshole and surface-wave measurements available in the alluvium in the city of Lisbon and the surrounding areas (Teves-Costa *et al.*, 2014) were not used here to directly estimate V_{S30} or soil type, as the published information provided only the average V_S. The values obtained in this study are similar to the ones known in downtown Lisbon, and they point also to soils of class C or D or S1, when the water table is shallower. The area covered by alluvial sediments encompasses several smaller cities such as Benavente, Samora Correia, Salvaterra de Magos, and parts of V. F. de Xira or Azambuja.

The alluvium close to the Tagus River between Lisbon and V. F. de Xira very probably falls into soil class E close to the Mesozoic outcrops, because the V_S in these rocks is above 800 m/s and in the sedimentary cover below 240 m/s. Using multiple geotechnical sounding datasets available in this area, we mapped the area where the alluvium thickness over the Mesozoic rocks varies approximately between 5 and 20 m, and therefore, the soil type belongs to class E. This area is part of the Greater Lisbon and is quite densely populated.

Pleistocene sediments present a large variability in V_{S30} and in soil types (compare Figs. 9 and 10 with Fig. 2). The range of V_{S30} is 184–835 m/s, and the range of the soil type varies from A (very low risk) to E (high risk). This is due to the great lithological variation in these sediments, which include sands, marls, clays, and gravels. Outcrops of the Pleistocene sediments occur mainly in the southern margin of the Tagus River, and the areas of higher risk are mostly occupied by agricultural terrains. Several villages and cities located over the Miocene terrains such as the district capital Santarém present some areas with relatively low V_{S30} values and a low-to-moderate risk.

Higher V_{S30} classes, with values exceeding 480 m/s, correspond to outcrops of Mesozoic, Miocene, and Pliocene, with the exception of a small area in the northern margin of the Tagus River at the north of the map, which falls into soil-type B. As stated above, some localities sited over Miocene outcrops correspond to moderate risk areas, with a V_{S30} class of 411–479 m/s and soil-type B. This is the case for the area where the district capital Santarém is situated, and other small-to-medium sized cities such as Vendas Novas, Torres Novas, or Tomar (the latter located slightly above the area shown in Figs. 9 and 10).

Conclusions

In the present research, V_P and V_S were obtained from seismic refraction profiles and a few crosshole measurements. These, together with geological and SPT information, allowed us to perform mechanical characterization of the uppermost geological formations in this region. Borehole data and detailed geological surveys at each site of seismic refraction profiling helped to interpret the profiles, overcome the refraction interpretation limitations such as velocity inversion and the presence of hidden layers, and together with raytracing confirm the maximum investigation depth reached in seismic refraction surveys. We compared refraction results with array AV measurements analyzed using high-resolution frequency–wavenumber, spatial autocorrelation methods, a combination of both methods, and with single-station AV using the H/V technique (HVSR), and we conclude that these methods can be used in the future to enhance the V_S database in this region, in particular array AV methods that consider the lateral or in depth variability of V_S, which is typical of shallow soils.

The near-surface characterization of the LTV led us to produce soil classification and V_{S30} maps, which are useful in assessing site effects and for microzonation purposes. From our results, we conclude that the study region is highly complex with spatially varying layer thicknesses and sharp lithological changes. Such high complexity prevents a simple geographical generalization/extension of the V_S and soil classification data points to geological formations. An approach was proposed to undertake this challenging task of extending the estimated data points (seismic velocity and soil types) to geological polygons. Although this approach is valid and seems to provide reasonably accurate results, the acquisition of additional velocity data and careful geological and lithostratigraphic analysis to produce more detailed V_{S30} and soil classification maps are essential to obtain better results in the future.

Nevertheless, the new V_{S30} and soil classification maps presented here show considerable details in 1:1 M or 1:500 K scales. They highlight a region of great susceptibility to earthquake shaking where part of the Greater Lisbon area and several small cities and villages are located. This region is mostly covered by Holocene alluvium, and in a smaller area, by Pleistocene conglomerates, sandstones, and claystones. Other areas are located over older geological formations such as the district capitals of Santarém, Setúbal, and as well as other small-to-medium sized cities, parts of which have a moderate-to-high risk. Other areas, where the Miocene and older rocks are close to the alluvium-covered surface, also have a high risk and should be mapped in more details in the future. Altogether, the presented information should contribute to an improvement in the evaluation of seismic risk and mitigation of earthquake damage in the LTV region, and to a better planning of land use and civil protection managing in case of occurrence of a destructive earthquake in the future.

Data and Resources

All raw seismic refraction data (SEG-2 files) acquired in the framework of this work can be obtained on request by con-

tacting Laboratório Nacional de Energia e Geologia (LNEG; www.lneg.pt) or the corresponding author. Digital geological data are owned by LNEG and are commercially available at http://geoportal.lneg.pt//index.php?lg=en&state=Inicio. Borehole reports are commercially available at http://geoportal.lneg.pt/geoportal/egeo/bds/tecnibase/ and can be obtained digitally (pdf) on request. *P*-wave seismic refraction data is only available on a LNEG internal report in Portuguese: the unpublished manuscript by J. Carvalho (1997), "Relatório Preliminar sobre Estudos de Refracção na Zona do Vale do Tejo", *LNEG Internal Report*. All websites were last accessed on August 2018.

Acknowledgments

The authors are grateful to the Portuguese Foundation for Science and Technology (FCT) for funding projects Strong Ground Motion and Near Field Effects in the Lower Tagus Region (NEFITAG) (PTDC-CTE/GIX/102245/2008), Site Condition Evaluation for National Seismic-Hazard Estimation (SCENE) (PTDC-CTE/GIX/103032/2008), and to S. Vilanova, Principal Investigator of project SCENE. The authors acknowledge also FCT for funding *P*-wave data acquisition in 1997 under project PBCIC/C/CTA/2107/95, "Characterization of Seismic Movements in the Lower Tagus Valley." They thank the European Union through the European Regional Development Fund under COMPETE 2020 through the ICT project (UID/GEO/04683/2013) under the reference POCI-01-0145-FEDER-007690. They are grateful to Luis Matias for helping with raytracing in a laterally varying media. The authors further acknowledge the field crew consisting of J. Gomes, F. Caneiras, and M. Silva. They are particularly grateful to Thomas Brocher and also to anonymous reviewers for valuable comments to improve this work.

References

ASTM International (2000). *Standard Guide for Using the Seismic Refraction Method for Subsurface Investigation*, D 5777-00, 1–14.

Baptista, M. A., and J. M. Miranda (2009). Evaluation of the 1755 earthquake source using tsunami modeling, in *The 1755 Lisbon Earthquake: Revisited*, L. Mendes Victor, C. Sousa Oliveira, J. Azevedo, and A. Ribeiro (Editors), Springer, Dordrecht, The Netherlands, 425–432, ISBN: 978-1-4020-8608-3.

Baptista, M. A., J. M. Miranda, and J. Batlló (2014). The 1531 Lisbon earthquake: A tsunami in the Tagus Estuary?, *Bull. Seismol. Soc. Am.* **104,** no. 5, 2149–2161.

Bauer, R. A., J. Kiefer, and N. Hester (2001). Soil amplification maps for estimating earthquake ground motions in the central US, *Eng. Geol.* **62,** 7–17.

Besana-Ostman, G. M., S. P. Vilanova, E. S. Nemser, A. Falcão-Flor, S. Heleno, H. Ferreira, and J. D. Fonseca (2012). Large Holocene earthquakes in the Lower Tagus valley fault zone, central Portugal, *Seismol. Res. Lett.* **83,** 67–76.

Bird, P. (2003). An updated digital model of plate boundaries, *Geochem. Geophys. Geosys.* **4,** no. 3, 1027, doi: 10.1029/2001GC000252.

Borcherdt, R. D. (1994). Estimates of site-dependent response spectra for design (methodology and justification), *Earthq. Spectra* **10,** 617–653.

Borcherdt, R. D. (2012). V_{S30}—A site-characterization parameter for use in building codes, simplified earthquake resistant design, GMPEs, and ShakeMaps, *15 WCEE Extended Abstract*, Lisbon, Portugal, 1–10.

Borges, J. F., M. Bezzeghoud, B. Caldeira, and J. Carvalho (2015). Ground-motion simulation in the Lower Tagus Valley basin, *Pure Appl. Geophys.* **172,** 2411–2420.

Borges, J. F., H. G. Silva, R. J. G. Torres, B. Caldeira, M. Bezzeghoud, J. A. Furtado, and J. Carvalho (2016). Inversion of ambient seismic noise HVSR to evaluate velocity and structural models of the Lower Tagus basin, Portugal, *J. Seismol.* **20,** 875–887.

Bourbie, T., O. Coussy, and B. Zinszner (1988). *Acoustics of Porous Media*, Gulf Publishing Company, Paris, France, 352 pp.

Brocher, T. M. (2005). Empirical relations between elastic wavespeeds and density in the Earth's crust, *Bull. Seismol. Soc. Am.* **95,** 2081–2092.

Brocher, T. M. (2008). Compressional and shear-wave velocity versus depth relations for common rock types in northern California, *Bull. Seismol. Soc. Am.* **98,** no. 2, 950–968.

Buforn, E., A. Udías, and M. A. Colombás (1988). Seismicity source mechanisms and tectonics of the Azores-Gibraltar plate boundary, *Tectonophysics* **152,** 89–118.

Building Seismic Safety Council (BSSC) (1994). *NEHRP Recommended Provisions for Seismic Regulations of New Buildings (FEMA 222A): Part I, provisions*, Federal Emergency Management Agency, Washington, D.C.

Building Seismic Safety Council (BSSC) (2001). *NEHRP Recommended Provisions for Seismic Regulations for New Buildings and Other Structures (FEMA-368), Part 1: Provisions*, 2000 Edition, Federal Emergency Management Agency, Washington, D.C.

Cabral, J., C. Moniz, J. Batló, P. Figueiredo, J. Carvalho, L. Matias, P. Teves-Costa, R. Dias, and N. Simão (2013). The 1909 Benavente (Portugal) earthquake: Search for the source, *Nat. Hazards* **69,** 1211–1227.

Cabral, J., C. Moniz, P. Ribeiro, P. Terrinha, and L. Matias (2003). Analysis of seismic reflection data as a tool for the seismotectonic assessment of a low activity intraplate basin—The Lower Tagus Valley (Portugal), *J. Seismol.* **7,** 431–447.

Cabral, J., P. Ribeiro, P. Figueiredo, N. Pimentel, and A. Martins (2004). The Azambuja fault: An active structure located in an intraplate basin with significant seismicity (Lower Tagus Valley, Portugal), *J. Seismol.* **8,** 347–362.

Canora, C., S. Vilanova, G. Besana-Ostman, J. Carvalho, S. Heleno, and J. Fonseca (2015). The eastern Lower Tagus Valley fault zone in central Portugal: Active faulting in a low-deformation region within a major river environment, *Tectonophysics* **660,** 117–131, doi: 10.1016/j.tecto.2015.08.026.

Carvalho, J., J. Cabral, R. Gonçalves, L. Torres, and L. Mendes-Victor (2006). Geophysical methods applied to fault characterization and earthquake potential assessment in the Lower Tagus Valley, Portugal, *Tectonophysics* **418,** 277–297.

Carvalho, J., R. Dias, C. Pinto, T. Cunha, J. Leote, S. Vilanova, J. Narciso, J. Borges, and R. Ghose (2013). Earthquake mitigation in the Lisbon and Lower Tagus Valley area, Portugal, *Thirteenth International Congress of the Brazilian Geophysical Society*, Rio de Janeiro, Brazil, 26–29 September, 4201.

Carvalho, J., H. Matias, L. Torres, R. Pereira, G. Manupella, and L. Mendes-Victor (2005). The structural and sedimentary evolution of the Arruda and Lower Tagus sub-basins, Portugal, *Mar. Petrol. Geol.* **22,** no. 3, 427–453.

Carvalho, J., T. Rabeh, M. Bielik, E. Szlaiova, L. Torres, M. Silva, F. Carrilho, L. Matias, and J. M. Miranda (2011). Geophysical study of the Ota–V.F. Xira–Lisboa–Sesimbra fault zone and of the Lower Tagus Cenozoic basin, *J. Geophys. Eng.* **8,** 395–411.

Castagna, J. P., M. L. Batzle, and R. L. Eastwood (1985). Relationships between compressional-wave and shear-wave velocities in clastic silicate rocks, *Geophysics* **50,** no. 4, 571–581.

Christensen, N. I. (1996). Poisson's ratio and crustal seismology, *J. Geophys. Res.* **101,** 3139–3156.

Dobrin, M. B., and C. H. Savitt (1989). *Introduction to Geophysical Prospecting*, McGraw-Hill, New York, New York, 890 pp.

Essien, U. E., A. O. Akankpo, and M. U. Igboekwe (2014). Poisson's ratio of surface soils and shallow sediments determined from seismic compressional and shear wave velocities, *Int. J. Geosci.* **5,** 1540–1546.

Eurocode 8 (2004). Design of structures for earthquake resistance, Part 1: General rules, seismic actions and rules for buildings, *European Standard EN 1998-1*, December 2004, European Committee for Standardization (CEN), Brussels, Belgium.

Fumal, T. E., and J. C. Tinsley (1985). Mapping shear wave velocities of near-surface geological materials, in *Predicting Aerial Limits of Earth-*

quake Induced Landsliding, in Evaluation of Earthquake Hazards in the Los Angeles Region—An Earth Science Perspective, J. I. Ziony (Editor), U.S. Geological Survey Paper 1360, 127–150.

Ghose, R., and M. Osada (1993). Anisotropy in near-surface formations and shear-wave birefringence—Its geotechnical implications: A VSP appraisal, *OYO Technical Report*, 55–145, ISSN: 0912–6325.

Grandin, R., J. F. Borges, M. Bezzeghoud, B. Caldeira, and F. Carrilho (2007a). Simulations of strong ground motion in SW Iberia for the 1969 February 28 ($M_s = 8.0$) and the 1755 November 1 (M* 8.5) earthquakes—II. Strong ground motion simulations, *Geophys. J. Int.* **171,** 807–822.

Grandin, R., J. F. Borges, M. Bezzeghoud, B. Caldeira, and F. Carrilho (2007b). Simulations of strong ground motion in SW Iberia for the 1969 February 28 ($M_s = 8.0$) and the 1755 November 1 (M* 8.5) earthquakes—I. Velocity model, *Geophys. J. Int.* **171,** 1144–1161.

Gregory, A. R. (1976). Fluid saturation effects on dynamic elastic properties of sedimentary rocks, *Geophysics* **41,** 895–921.

Gutscher, M. A., S. Dominguez, G. K. Westbrook, P. Le Roy, F. Rosas, J. C. Duarte, P. Terrinha, J. M. Miranda, D. Graindorge, A. Gailler, *et al.* (2012). The Gibraltar subduction: A decade of new geophysical data, *Tectonophysics* **574/575,** 72–91, doi: 10.1016/j.tecto.2012.08.038.

Herak, M. (2008). ModelHVSR—A Matlab® tool to model horizontal-to-vertical spectral ratio of ambient noise, *Comput. Geosci.* **34,** 1514–1526.

Hunt, R. E. (2006). *Geotechnical Investigation Methods: A Field Guide for Geotechnical Engineers*, CRC Press (Taylor & Francis Group), Boca Raton, Florida.

International Council of Building Officials (ICBO) (1997). *Uniform Building Code*, International Council of Building Officials. Whittier, California.

Johnston, A. C., and L. R. Kanter (1990). Earthquakes in stable continental crust, *Sci. Am.* **262,** 68–75.

Justo, J. L., and C. Salwa (1998). The 1531 Lisbon earthquake, *Bull. Seismol. Soc. Am.* **88,** 319–328.

Kalkan, E., C. J. Wills, and M. David Branum (2010). Seismic hazard mapping of California Considering site effects, *Earthq. Spectra* **26,** 1039–1055.

Kanlı, A. I., P. Tildy, Z. Prónay, A. Pınar, and L. Hermann (2006). V_{S30} mapping and soil classification for seismic site effect evaluation in Dinar region, SW Turkey, *Geophys. J. Int.* **165,** 223–235.

Kilty, K. T., R. A. Norris, W. R. McLamore, K. R. Hennon, and K. Euge (1986). Seismic refraction at Horse Mesa Dam: An application of the generalized reciprocal method, *Geophysics* **51,** 266–275.

Knödel, K., G. Lange, and V. Hans-Jürgen (2007). *Environmental Geology: Handbook of Field Methods and Case Studies*, Springer, Berlin, Germany.

Konstantaki, L. A., R. Ghose, D. Draganov, and T. Heimovaara (2016). Wet and gassy zones in a municipal landfill from *P*- and *S*-wave velocity fields, *Geophysics* **81,** EN75–EN86.

Lankston, R. W. (1989). The seismic refraction method: A viable tool for mapping shallow targets into the 1990s, *Geophysics* **54,** 1535–1542.

Lankston, R. W. (1990). High-resolution refraction seismic data acquisition and interpretation, in *Geotechnical and Environmental Geophysics*, S. H. Ward (Editor), Investigations in Geophysics Number 5, Society of Exploration Geophysicists, Tulsa, Oklahoma, 45–73.

Laboratório Nacional de Energia e Geologia (LNEG) (2010). *Geological Map of Portugal Scale 1: 1,000,000*, Laboratório Nacional de Energia e Geologia, Alfragide, Portugal.

Matsuoka, M., K. Wakamatsu, K. Fujimoto, and M. Saburoh (2005). Average shear-wave velocity mapping using Japan engineering geomorphologic classification map, *J. Struct. Mech. Earthq. Eng.* **794/I-72,** 239–251.

Maunde, A., and N. E. Bassey (2017). Seismic refraction investigation of fracture zones and bedrock configuration for geohydrologic and geotechnical studies in part of Nigeria's Capital City, Abuja, *J. Earth Sci. Geotech. Eng.* **7,** 91–102.

Mendes-Victor, L. A., C. S. Oliveira, J. Azevedo, and A. Ribeiro (Editors) (2009). *The 1755 Lisbon Earthquake: Revisited*, Springer, Berlin, Germany.

Mendes-Victor, L. A., C. S. Oliveira, I. Pais, and P. Teves-Costa (1994). Earthquake damage scenarios in Lisbon for disaster preparedness, in *Issues in Urban Risk*, NATO ASI Series, Vol. 271, Springer, Dordrecht, The Netherlands, 265–289.

Motazedian, D., J. A. Hunter, A. Pugin, and H. Crow (2011). Development of a V_{S30} (NEHRP) map for the city of Ottawa, Ontario, Canada, *Can. Geotech. J.* **48,** 458–472.

Nakamura, Y. (1989). A method for dynamic characteristics estimation of subsurface using microtremor on the ground surface, *Q. Rep. Railway Tech. Res. Inst.* **30,** 25–33.

Northwood, E. J. (1967). Errors in refraction interpretation, in *Seismic Refraction Prospecting*, A. W. Musgrave (Editor), Society of Exploration Geophysicists, Tulsa, Oklahoma, 458–466.

Pais, J., P. P. Cunha, D. Pereira, P. Legoinha, R. Dias, D. Moura, A. B. Silveira, J. C. Kullberg, and J. A. González-Delgado (2012). *The Paleogene and Neogene of Western Iberia (Portugal): A Cenozoic Record in the European Atlantic Domain*, Springer, New York, New York, 156 pp.

Palmer, D. (1980). *The Generalized Reciprocal Method of Seismic Refraction Interpretation*, Society of Exploration Geophysicists, Tulsa, Oklahoma, 104 pp.

Palmer, D. (1981). An introduction to the generalized reciprocal method of seismic refraction interpretation, *Geophysics* **46,** 1508–1518.

Penelis, G. G. (1997). Eurocode 8: Characterization of seismic action, design spectra, future trends, *Proc. of SERINA—Seismic Risk: An Integrated Seismological, Geotechnical and Structural Approach*, Thessaloniki, Greece, 479–492.

Perrin, N. D., D. Heron, A. Kaiser, and C. Van Houtte (2015). V_{S30} and NZS 1170.5 site class maps of New Zealand, *2015 NZSEE Conference*, Rotorua, New Zeeland, *10–12 April*, Paper 0–07.

Pickering, D. J. (1970). Anisotropic elastic parameters for soil, *Geotechnique* **20,** 271–276.

Pitilakis, K., E. Riga, and A. Anastasiadis (2012). Design spectra and amplification factors for Eurocode 8, *Bull. Earthq. Eng.* **10,** 1377–1400.

Pitilakis, K., E. Riga, and A. Anastasiadis (2015). New design spectra in Eurocode 8 and preliminary application to the seismic risk of Thessaloniki, Greece, in *Perspectives on Earthquake Geotechnical Engineering*, A. Ansal and M. Sakr (Editors), Springer, Basel, Switzerland.

Rafek, A.-G. (1989). Depth of penetration of geophysical exploration methods as applied in shallow geological engineering investigations, *Bull. Seismol. Soc. Malaysia* **23,** 21–28.

Salem, H. S. (2000a). The compressional to shear-wave velocity ratio for surface soils and shallow sediments, *Eur. J. Environ. Eng. Geophys.* **5,** 3–14.

Salem, H. S. (2000b). Poisson's ratio and the porosity of surface soils and shallow sediments, determined from seismic compressional and shear wave velocities, *Geotechnique* **50,** no. 4, 461–463.

Sanz, A. G., and A. M. Contreras (2005). Nova Travessia do Tejo, *Ensaios sísmicos cross-hole Sondagen S-304*, Private Report of International Geophysical Technology for Geocontrole (in Spanish).

Silva, V., H. Crowley, H. Varum, and R. Pinho (2015). Seismic risk assessment for mainland Portugal, *Bull. Earthq. Eng.* **13,** 429–457.

Simões, M. (1998). Contribuição para o Conhecimento Hidrogeológico do Cenozóico na Bacia do Baixo Tejo, *Ph.D. Thesis*, Universidade Nova de Lisboa, Portugal (in Portuguese).

Stuempel, H., S. Kaehler, R. Meissner, and B. Milkereit (1984). The use of seismic shear waves and compressional waves for lithological problems of shallow sediments, *Geophys. Prospect.* **32,** 662–675.

Sucuoğlu, H., and S. Akkar (2014). *Basic Earthquake Engineering: From Seismology to Analysis and Design*, Springer, Basel, Switzerland.

Tatham, R. H. (1982). V_P/V_S and lithology, *Geophysics* **47,** 336–344.

Teves-Costa, P., and J. Batlló (2011). The 23 April 1909 Benavente earthquake (Portugal): Macroseismic field revision, *J. Seismol.* **15,** 59–70.

Teves-Costa, P., I. M. Almeida, I. Rodrigues, R. Matildes, and C. Pinto (2014). Geotechnical characterization and seismic response of shallow geological formations in downtown Lisbon, *Ann. Geophys.* **57,** no. 4, doi: 10.4401/ag-6390.

Teves-Costa, P., I. Rodrigues, R. J. G. Torres, J. Carvalho, I. M. Almeida, and J. F. Borges (2013). V_{S30} estimation using ambient vibrations and seismic refraction experiments—Application to the Lower Tagus

Valley (Portugal), *Abstracts of the Joint Assembly IAHS-IAPSO-IAPSEI*, Gotemburg, Sweden, 22–26 July.

Turesson, A. (2007). A comparison of methods for the analysis of compressional, shear, and surface wave seismic data, and determination of the shear modulus, *J. Appl. Geophys.* **61,** no. 2, 83–91.

Uyanik, O. (2010). Compressional and shear-wave velocity measurements in unconsolidated top-soil and comparison of the results, *Int. J. Phys. Sci.* **5,** 1034–1039.

Veludo, I., N. A. Dias, P. E. Fonseca, L. Matias, F. Carrilho, C. Haberland, and A. Villaseñor (2117). Crustal seismic structure beneath Portugal and southern Galicia (western Iberia) and the role of Variscan inheritance, *Tectonophysics* **717,** 645–664.

Vilanova, S., J. Narciso, J. Carvalho, I. Lopes, M. Q. Ferreira, C. Cancela, R. Moura, E. Nemser, and J. Borges (2018). Developing a geologically-based V_{S30} site-conditions model for Portugal: Methodology and assessment of the performance of proxies, *Bull. Seismol. Soc. Am.* **108,** no. 1, 322–337.

Vilanova, S. P., E. Nemser, G. M. Besana-Ostman, M. Bezzeghoud, J. F. Borges, A. Brum da Silveira, J. Cabral, J. Carvalho, P. P. Cunha, R. P. Dias, *et al.* (2014). Incorporating Descriptive metadata into seismic source zone models for seismic hazard assessment: A case study of the Azores-West Iberian region, *Bull. Seismol. Soc. Am.* **104,** 1212–1229.

Wald, D. J., and T. I. Allen (2007). Topographic slope as a proxy for seismic site conditions and amplification, *Bull. Seismol. Soc. Am.* **97,** 1379–1395.

Wathelet, M. (2005). Array recordings of ambient vibrations: Surface-wave inversion, *Ph.D. Thesis*, University of Liège, Belgium.

Wills, C. J., and K. B. Clahan (2006). Developing a map of geologically defined site-condition categories for California, *Bull. Seismol. Soc. Am.* **96,** 1483–1501.

Wills, C., M. Petersen, W. Bryant, M. Reichle, G. Saucedo, S. Tan, G. Taylor, and J. A. Treiman (2000). Site-conditions map for California based on geology and shear-wave velocity, *Bull. Seismol. Soc. Am.* **90,** S187–S208.

Wills, C. J., C. I. Gutierrez, F. G. Perez, and D. M. Branum (2015). A next generation V_{S30} map for California based on geology and topography, *Bull. Seismol. Soc. Am.* **105,** 3083–3091.

Zelt, C. A., and R. B. Smith (1992). Seismic traveltime inversion for 2-D crustal velocity structure, *Geophys. J. Int.* **108,** 16–34.

Appendix A

Table A1 shows information on all data points used to elaborate the soil classification and V_{S30} maps presented in this work.

Appendix B

Comparison with Seismic Ambient Vibration and Crosshole Measurements

At three locations (see locations in Fig. 2), seismic refraction velocities were compared with ambient vibration (AV) measurements using an array (Teves-Costa *et al.*, 2013), or a single station (Borges *et al.*, 2016), or unpublished crosshole *S*-wave data. At Salvaterra de Magos (SM), Samora Correia (SC), and Vila Franca de Xira (VFX), refraction velocities were tested with AV measurements (Teves-Costa *et al.*, 2013; Borges *et al.*, 2016), whereas between SC and Benavente, unpublished crosshole data (Sanz and Contreras, 2005) acquired for the construction of a large engineering structure were used (Fig. 6, see crosshole locations in Fig. 2).

Array AV measurements were analyzed using high-resolution frequency–wavenumber (HRFK), spatial autocorrelation (SPAC) methods, and a combination of both methods (HRFK and SPAC) to estimate the phase-velocity dispersion curves (Teves-Costa *et al.*, 2013). These curves were afterward inverted using the improved neighbourhood algorithm (Wathelet, 2005) to obtain the V_S profiles. Array data were collected using 15 seismic stations azimuthally distributed in a concentric circular geometry, and four arrays with radius of 5, 10, 20, and 40 m were performed, each with a central station. First, the two outer rings were recorded simultaneously and afterward the 15 stations were moved to the two inner circumferences. Record length was 1 hr 30 min for the 5 and 10 m arrays, and varied between 2 hrs and 2 hrs 30 min for the 20 and 40 m arrays. Seismic stations RefTek RT-125A-GS-11D (4.5 Hz vertical seismometers) were used in recording the data. Single-station measurements were processed using the horizontal-to-vertical spectral ratio (HVSR) technique (Nakamura, 1989), and the inversion used the software ModelHVSR (Herak, 2008) to obtain the V_S model. A detailed explanation of the used method can be found in Borges *et al.* (2016). Crosshole data were acquired with a Geotomographie equipment, a multicomponent receiver BGK-7 and a Strata-View R-24 seismic acquisition system to a depth of 57 m.

Figure B1 compares V_S profiles obtained using AV and the seismic refraction method at the three sites: (a) SM, (b) SC, and (c) VFX. At each site, the AV and the refraction measurements were separated by a few tens of meter distance due to logistic reasons. From Figure B1, we can draw the following conclusions: (1) the refraction velocity values are placed within the range of velocities obtained from the different AV methods; (2) the AV methods appear to offer relatively greater investigation depths (at least 40 m); (3) AV array methods present greater vertical resolution than HVSR and refraction methods and are able to detect the velocity gradients with depth which, according to borehole data used here and elsewhere (Carvalho *et al.*, 2005), characterize the Cenozoic formations; (4) HVSR and refraction methods provide a similar V_S structure, and they differ by less than 20% below 10 m depth, but large velocity differences are found in the topmost 10 m; (5) AV array methods give very similar V_S structure (depth distribution) and V_S values to those obtained by HVSR and refraction methods; the difference is less than 10% except at certain locations (e.g., SC site) where the difference is much greater.

To explain the apparent discrepancies in (4) and (5) mentioned above, careful geological studies were carried out at each acquisition site to check the geological formation/lithology, because the location of the comparison site had been marked on a geological map of 1:50 K scale and each method had been acquired with a few days of interval and a few tens of meters from each other. It was found that only at VFX site the data had been acquired exactly over the same geological

Table A1

Layer Depths, Shear-Wave Velocities, and V_{S30} for Each Data Point Used in This Work

Profile	ID	Geology	Lithologies	Age	V_{S1}	V_{S2}	V_{S3}	D_2	D_3	V_{S30}	EC8 Soil Class	X	Y
TOJ1	1	Alluvium	Clays	Holocene	99	408	—	16	—	153	S1	487,699	4,298,820
VFX5	2	Alluvium	Clays	Holocene	84	222	372	5	12	215	C	502,206	4,314,062
PM12	3	Alluvium	Clays	Holocene	247	322	—	8	—	297	C	522,254	4,328,389
RS15	4	Alluvium	Clays	Holocene	164	276	—	11	—	220	C	528,950	4,344,254
ARR23	5	Alluvium	Clays	Holocene	172	665	—	15	—	274	C	551,086	4,366,760
BEN31	6	Alluvium	Clays	Holocene	150	233	—	14	—	185	C	516,293	4,315,416
PAN46	7	Alluvium	Clays	Holocene	121	250	—	10	—	186	C	506,359	4,299,604
PSE49	8	Alluvium	Clays	Holocene	96	142	—	10	—	123	S1	514,054	4,307,723
PV47	9	Alluvium	Clays	Holocene	317	356	—	28	—	318	C	510,101	4,298,950
VFX34	10	Alluvium	Clays	Holocene	152	531	—	0.2	—	522	B	500,976	4,311,552
PS34	11	Alluvium	Clays	Holocene	89	267	—	1	—	246	C	503,272	4,314,746
PS40	12	Alluvium	Clays	Holocene	21	431	—	1	—	296	C	487,704	4,299,103
PS22	13	Alluvium	Clays	Holocene	166	276	—	4	—	254	C	530,684	4,345,553
PS32	14	Alluvium	Clays	Holocene	74	162	226	1	3	211	C	505,912	4,297,349
PS25	15	Alluvium	Sands, clays	Holocene	302	442	818	3	27	445	B	521,221	4,328,184
PS19	16	Alluvium	Clays	Holocene	63	375	—	1	—	301	C	509,782	4,314,809
PS3	17	Alluvium	Clays	Holocene	228	656	—	5	—	488	B	551,529	4,366,635
A10	18	Alluvium	Clays	Holocene	406	617	—	6	—	555	B	512,053	4,313,118
Cross-232	19	Alluvium	Clays	Holocene	173	195	200	6	22	191	C	511,336	4,313,460
Cross-304	20	Alluvium	Clays	Holocene	181	184	211	11	19	192	C	512,126	4,313,102
SAM12	21	Alluvium	Sands, clays	Holocene	319	444	—	6	—	410	B	515,015	4,311,247
TV1	22	Alluvium	Landfill, silty sand	Holocene	169	202	525	7.5	24	221	C	487,983	4,284,795
TV2	23	Alluvium	Landfill, silty sand	Holocene	167	207	525	3	22	240	C	488,119	4,284,604
TV3	24	Alluvium	Landfill, silty clay	Holocene	172	177	—	7	—	176	D	488,056	4,284,374
PS29	25	Undifferentiated sands and gravels	Sands, gravel	Pleistocene	388	550	569	3	8	540	B	513,202	4,308,312
PS17	26	Undifferentiated sands and gravels	Sands, gravel	Pleistocene	70	166	501	0.4	4	371	B	530,249	4,331,858
PS14	27	Undifferentiated sands and gravels	Sands, gravel	Pleistocene	98	230	864	2	8	429	E	538,633	4,346,258
PS20	28	Undifferentiated sands and gravels	Sands, gravel	Pleistocene	162	361	965	2	6	621	E	519,941	4,318,226
BEN3	29	Fluvial terrace deposits	Sands, gravel	Pleistocene	299	467	—	11	—	384	B	516,428	4,314,971
PS39	30	Fluvial terrace deposits	Sands, gravel	Pleistocene	244	348	564	17	7	489	B	487,855	4,299,979
PS31	31	Fluvial terrace deposits	Sands, gravel	Pleistocene	267	401	465	1	9	436	B	510,584	4,299,254
PS30	32	Fluvial terrace deposits	Sands, gravel	Pleistocene	278	376	441	1	11	413	C	514,314	4,304,474
FBE37	33	Undifferentiated sands and gravel	Sands, gravel	Pleistocene	139	406	861	1	5	636	E	529,731	4,331,898
SAM41	34	Undifferentiated sands and gravels	Sands, gravel	Pleistocene	146	246	—	15	—	184	C	519,231	4,317,469
TOJ2	35	Fluvial terrace deposits	Sands, gravel	Pleistocene	350	513	—	9	—	447	B	487,652	4,299,560
ONO6	36	Fluvial terrace deposits	Sandstones	Pleistocene	225	284	543	17	36	247	C	503,163	4,320,894
PO18	37	Fluvial terrace deposits	Sands, gravel	Pleistocene	211	443	—	5	—	379	B	534,564	4,353,250
BO20	38	Fluvial terrace deposits	Sands, gravel	Pleistocene	264	932	1516	3	22	836	A	539,013	4,356,174
EN21	39	Fluvial terrace deposits	Gravel, sands	Pleistocene	385	1157	—	19	—	515	B	540,152	4,363,890
STE44	40	Fluvial terrace deposits	Sands, gravel	Pleistocene	509	643	—	20	—	549	B	523,382	4,302,023
BEL33	41	Porto Carro marls	Sands, marls	Pleistocene	284	372	—	8	—	344	C	488,228	4,272,651
PS18	42	Fluvial terrace deposits	Sands, gravel	Quaternary	319	266	—	1	—	267	B	528,776	4,322,458

(*continued*)

Table A1 (*Continued*)

Profile	ID	Geology	Lithologies	Age	V_{S1}	V_{S2}	V_{S3}	D_2	D_3	V_{S30}	EC8 Soil Class	X	Y
PS10	43	Fluvial terrace deposits	Sands, gravel	Quaternary	178	204	553	0.4	7	397	B	540,260	4,356,117
PS4	44	Fluvial terrace deposits	Gravel, sands	Quaternary	414	659	—	2	—	630	A	545,759	4,366,592
CRA27	45	Ulme Formation	Sandstones, gravel	Plio-Pleistocene	277	391	—	8	—	350	C	488,298	4,362,498
CHO17	46	Ulme Formation	Sandstones, gravel	Pliocene	693	833	—	28	—	700	B	534,564	4,353,250
AZ10	47	Ulme Formation	Sandstones, gravel	Pliocene	269	492	—	12	—	372	B	511,081	4,326,466
CCP11	48	Ulme Formation	Sandstones	Pliocene	421	944	—	17	—	557	B	516,277	4,330,587
VCO13	49	Ulme Formation	Sandstones	Pliocene	459	671	—	1	—	661	B	521,630	4,337,261
ACT13	50	Ulme Formation	Sandstones	Pliocene	398	402	—	5	—	401	B	503,326	4,289,203
VER2	51	Ulme Formation	Sandstones	Pliocene	103	366	502	1	41	338	C	486,397	4,270,377
SET14	52	Ulme Formation	Sandstones, claystones	Pliocene	219	350	—	9	—	298	C	511,518	4,265,598
PS26	53	Ulme Formation	Sandstones	Pliocene	184	509	944	0.4	26	528	B	516,495	4,330,484
PS33	54	Ulme Formation	Sandstones	Pliocene	138	493	797	1	9	608	B	517,648	4,295,640
PS24	55	Ulme Formation	Sandstones	Pliocene	103	371	624	0.5	4	538	A	520,961	4,337,116
ALC19	56	Tomar Clays Formation	Sandstones with carbonate crusts	Upper Miocene	240	355	561	5	29	335	C	536,019	4,363,618
PS21	57	Undifferentiated Alcoentre Formation and Tomar Clays Formation	Sandstones, limestones	Upper Miocene	338	778	1227	2	10	905	B	523,223	4,301,748
PS49	58	Lisbon Miocene (Marvila limestones)	Sandstones, limestones	Upper Miocene	681	1649	—	3	—	1437	E	492,085	4,298,740
PS48	59	Lisbon Miocene (Areolas de Braço de Prata)	Sandstones, limestones	Upper Miocene	238	410	1048	2	6	735	E	492,027	4,297,198
PS47	60	Lisbon Miocene (Vale de Chelas sands)	Sandstones, limestones	Upper Miocene	180	388	1292	1	5	831	B	490,937	4,298,888
PS9	61	Undifferentiated Alcoentre Formation and Tomar Clays Formation	Claystones, sandstones with carbonate crusts	Upper Miocene	249	821	—	2	—	689	B	531,257	4,352,402
PS8	62	Undifferentiated Alcoentre Formation and Tomar Clays Formation	Claystones, sandstones with carbonate crusts	Upper Miocene	178	456	—	3	—	402	B	531,767	4,353,363
PS7	63	Tomar Clays Formation	Sandstones with carbonate crusts	Upper Miocene	158	349	398	1	5	370	B	535,479	4,362,720
APL3	64	Banco Real Formation	Sandstones, limestones, gravel	Lower-Middle Miocene	227	580	717	3	48	509	B	488,086	4,296,941
APL4	65	Musgueira limestones	Sandstones, limestones	Lower-Middle Miocene	445	846	—	2	—	791	B	489,127	4,296,939
PS41	66	Banco Real Formation	Sandstones, limestones, gravel	Lower-Middle Miocene	259	513	774	1	8	658	B	488,348	4,297,003
SAN26	67	Alcoentre Formation	Sandstones, claystones	Miocene	284	449	—	7	—	392	B	526,591	4,343,881
SVF30	68	Lisbon Miocene (Areias com placuna miocénica)	Sandstones, claystones	Miocene	316	524	713	6	43	336	C	488,966	4,285,090
CAR7	69	Alcoentre Formation	Sandstones, claystones with carbonate crusts	Miocene	261	405	805	2	24	429	B	500,544	4,320,696
CHE8	70	Alcoentre Formation	Sandstones, claystones	Miocene	236	305	—	6	—	289	C	501,456	4,324,912
AZ9	71	Alcoentre Formation	Claystones, sandstones	Miocene	400	574	—	6	—	526	B	512,004	4,327,116

(*continued*)

Table A1 (*Continued*)

Profile	ID	Geology	Lithologies	Age	V_{S1}	V_{S2}	V_{S3}	D_2	D_3	V_{S30}	EC8 Soil Class	X	Y
SAN14	72	Alcoentre Formation	Sandstones, claystones with carbonate crusts	Miocene	148	318	512	1	38	303	C	527,461	4,344,376
VF16	73	Undifferentiated Alcoentre Formation and Tomar Clays Formation	Sandstones, claystones with carbonate crusts	Miocene	171	406	697	2	22	415	B	530,853	4,352,829
PS28	74	Alcoentre Formation	Sandstones, claystones	Miocene	265	296	480	2	7	417	A	501,483	4,325,144
PS27	75	Alcoentre Formation	Claystones, sandstones, with carbonate crusts	Miocene	291	1069	—	2	—	921	C	511,567	4,327,203
PS23	76	Alcoentre Formation	Sandstones, claystones with carbonate crusts	Miocene	250	283	—	1	—	282	B	527,266	4,344,418
PS42	77	Alcoentre Formation	Sandstones, claystones with carbonate crusts	Miocene	136	332	654	1	9	477	A	500,538	4,320,758
CNX29	78	Volcanic complex of Lisbon	Weathered basalt	Cretaceous	186	500	2096	2	10	781	B	479,457	4,285,729
PS35	79	Volcanic complex of Lisbon	Weathered basalt	Cretaceous	167	620	1894	1	8	1039	A	483,694	4,303,288
PS45	80	Freixial, Sobral e Arranhó Formation	Sandstones, limestones	Upper Jurassic	271	1077	—	1	—	998	C	483,826	4,306,839
PS43	81	Abadia Formation	Claystones, sandstones	Upper Jurassic	164	536	—	7	—	345	B	500,985	4,316,549
PS1	82	Gneisso-migmatitic Formation	Gneisses	Precambrian	75	1240	—	1	—	720	C	556,355	4,367,817

Geology indicates the geological formation mapped at the 1:50 K scale where the profile was acquired. V_{Si}, S-wave velocity for layer i in m/s; Di, depth to layer i in meters; Soil, soil class according to Eurocode 8 (2004). X and Y are data point coordinates in the UTM system, zone 29, datum WGS84 are in meters. Data points starting with PS indicate refraction profiles whose S-wave velocity was extrapolated from P-wave velocity using the approach presented in this article. TVj, data published by Teves Costa *et al.* (2014); $j = 1$, Lisbon downtown north; $j = 2$, Lisbon downtown center; $j = 3$, Lisbon downtown south.

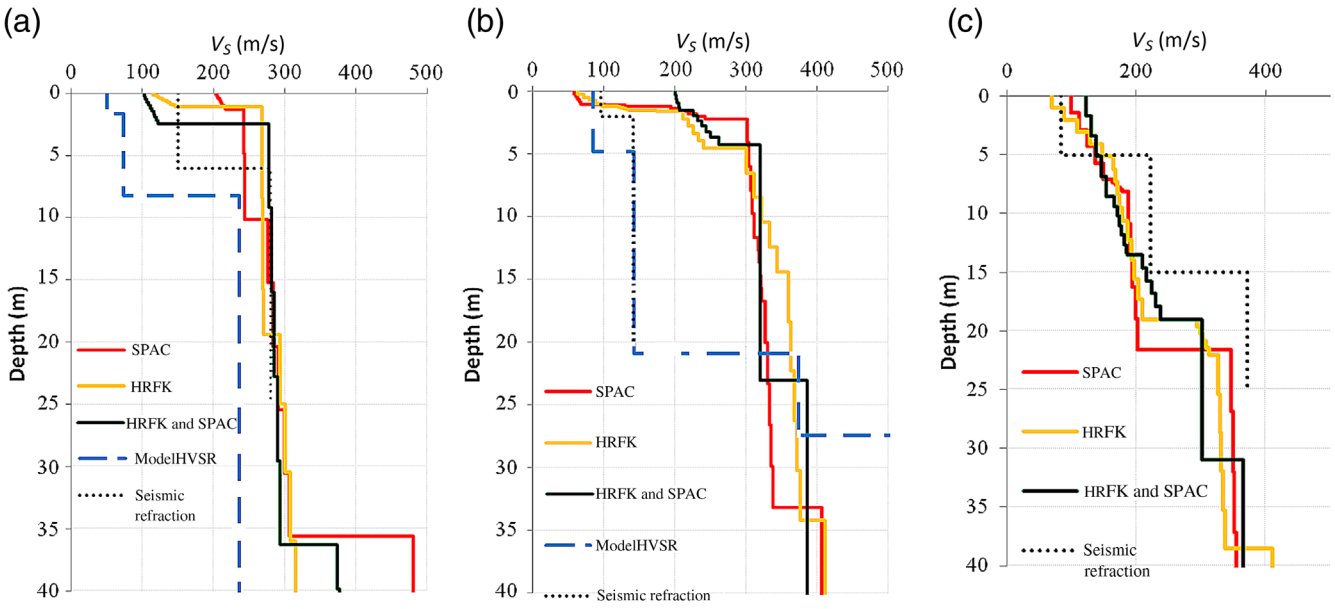

Figure B1. Comparison of seismic refraction results with ambient vibration (AV) measurements analyzed using high-resolution frequency–wavenumber (HRFK) method, spatial autocorrelation (SPAC), single-station horizontal-to-vertical (H/V) spectral ratio (HVSR) method and combined HRFK and SPAC at three different sites: (a) Salvaterra, (b) Samora Correia, (c) and Vila Franca Xira (after Teves-Costa *et al.*, 2013). The color version of this figure is available only in the electronic edition.

formation and lithology, that is, clayey alluvium. At SM (Fig. B1a), the refraction profile was acquired over Pleistocene undifferentiated sands and gravels formation, while the AV data were collected over Holocene alluvium. The refraction data collected here (see Seismic Velocity/Depth Data, Velocity Model Results, and Deriving V_{S30} and Soil Classification Maps sections) show that these two geological formations have different average velocities.

At SC comparison test site (Fig. B1b), the refraction profile was also acquired over alluvium but the AV data were collected over fluvial terrace deposits formation of Pleistocene, which, according to the results of refraction data analyses, have a large range of V_S value depending on the lithology. This explains the discrepancy observed in Figure B1b between the AV array method and the refraction profile. The similarity in the first 20 m between the results of single-station AV method and the seismic refraction method can possibly be judged as a coincidence, as we discuss in detail in the next paragraph.

Indeed, it should be noted that the refraction velocities presented in Figure B1 correspond to average velocities obtained from five shot points covered at each profile location. For example, in the refraction profile acquired at SM (Fig. B1a), the V_S values in the second layer range from 216 to 294 m/s. This range encompasses the velocities measured in the AV methods, which represent V_S values averaged at a single-station and at an array that differs in location by a few tens of meters, as mentioned above. However, if we take into consideration the natural variability of V_S in shallow soils, some differences between single-station AV, array AV and refraction methods are expected. Taking this into consideration, array AV and refraction methods are preferable to single-station AV or crosshole methods, as the latter are more representative of the average velocity of the site. We believe that the similarity of V_S values in the first 20 m at SC (Fig. B1b) between these methods is a coincidence. The lower performance of the HVSR method, which is clear at the SM site and where this method presents clearly different results compared to refraction and array AV methods, is due to the 1D assumption made in the HVSR method.

We conclude that the observed velocity difference between the refraction and the array AV methods is due to difference in the sampled lithologies. Based on results from datasets from our comparison sites, for a particular lithology this velocity difference is less than 20%, and this can be attributed to methodological difference and small difference in lithologies at the survey locations. In single-station methods, the V_S variability in the subsoil is ignored. Our comparison results highlight the importance of having an accurate location while acquiring/using shear-wave datasets and a correct assessment of the near-surface geology/lithology.

Finally, we compare between crosshole and refraction seismic velocities obtained in the area between Samora and Benavente, at two locations that are separated by about 70 m apart. Figure 6 shows the refraction model of profile A10 and the nearby crosshole measurements (entry 18 in Table A1). Crosshole seismic measurements were carried out before the construction of the highway A10 (in 2005) that required these studies, whereas the seismic refraction profile was acquired afterward in 2013 over a landfill (made of very compacted limestone gravel) that was created at the time of the highway construction. Therefore, the refraction seismic velocity of the first layer corresponds to the compacted landfill and is much higher than the one obtained by the crosshole method. The velocity of the second layer in the refraction model (~600 m/s at 8 m depth) is, however, also much higher than the measured velocity (about 200 m/s) at the same depth in the two crosshole surveys. Though the surface material surrounding the landfill where the refraction profile was acquired is more clayey than the site where the crosshole measurements were made, the higher velocity at the refraction site is possibly due to the sediment compaction at the landfill and the loading due to the constructed highway.

Laboratório Nacional de Energia e Geologia
Estrada Portela-Zambujal
Apartado 7586-Alfragide
2610-999 Amadora, Portugal
joao.carvalho@lneg.pt
ruben.dias@lneg.pt
cdcpinto@gmail.com
jaime.leote@lneg.pt
(J.C., R.D., C.P., J.L.)

Department of Geoscience and Engineering
Delft University of Technology
P.O. Box 5028
2628 GA Delft, The Netherlands
r.ghose@tudelft.nl
(R.G.)

Instituto Dom Luiz
Faculdade de Ciências
Universidade de Lisboa
1749-016 Lisbon, Portugal
mpcosta@fc.ul.pt
(P.T.-C.)

Institute of Earth Sciences
University of Évora
R. Romão Ramalho, 59
7000 Évora, Portugal
jborges@uevora.pt
(J.B.)

Instituto Superior Técnico
R. Rodovisco Pais, 1
1040-001 Lisbon, Portugal
joao.narciso@tecnico.ulisboa.pt
(J.N.)

Manuscript received 14 November 2017;
Published Online 11 September 2018